Characterization of Heavy-Ion-Background in Jet-Reconstruction

Charakterisierung des Untergrundes für die Jet-Rekonstruktion in Schwerionenkollisionen

Bachelor Thesis of Hendrik Poppenborg

Westfälische Wilhelms-Universität Münster

Fachbereich Physik

- September 2011 -

Erstgutachter: Dr. Christian Klein-Bösing

Zweitgutachter: Prof. Dr. Johannes P. Wessels

Contents

1 Introduction

The topic of this bachelor thesis is the characterization of the background fluctuations occurring in the analysis of heavy-ion collisions that are currently carried out at the Large Hadron Collider (LHC) provided by CERN.

With energies of more than 2 TeV per nucleon pair, the collisions of lead ions are supposed to create a state of high temperature and compression that was not reached until now. The purpose is to examine the so called quark-gluon plasma (QGP), a state of baryonic matter that presumably prevailed in the early stage after the Big Bang. Regarding the collisions in the experiment, this high level of energy implies a large amount of scattered particles that are to be detected, namely by the ALICE detector system. With this data it is possible to deduce the properties of the scattered partons (quarks and gluons) which were involved right after the collisions and travel through the created QGP. To accomplish this deduction the detected particles can be merged under certain criteria and form so called jets that, if appropriately computed, contain the momenta of the primary partons. This is well established in proton-proton (pp) collisions, but suffers from further complication in the heavy-ion environment. The way of how the jet properties are computed is given by jet reconstruction algorithms.

To supply the basic knowledge needed in this thesis, a theoretical overview will introduce the reader to the concept of jets, jet reconstruction and related terms. The Gamma distribution will be introduced which will provide a tool for the parametrization of jet background fluctuations later on. After that a short overview follows about the ALICE project and the research of the QGP. The current approach to the issue of background fluctuations is going to be presented and subsequently, the actual analysis of this work.

2 Theoretical Overview

2.1 Jets

In collisions of highly accelerated ions, the protons and neutrons no longer scatter as whole particles. Instead, the constituting partons, namely the gluons and quarks, scatter elastically with each other gaining a high momentum that is transverse to the beam direction. Since they are subject to the Strong Interaction, the scattered partons will lead to further particle production as the potential energy between partons increases with the distance. The phenomenon that all color charged particles ultimately hadronize is referred to as Hadronic Confinement. As long as the energy is sufficient, the created partons themselves will create new partons which will lead to a collimated spray of particles that arise from the point of collision in the direction of the primarily scattered parton. In particle physics this is called a jet. As they contain the momentum and energy of the originally scattered parton, they are a main subject of research at every collider experiment. That said, the definition of a particle jet seems clear, but in reality it is not, because there are no final criteria for assigning detected particles to a jet.

2.2 Jet Reconstruction

In order to reconstruct jets, so called jet reconstruction algorithms are employed. Today one can choose out of a variety of algorithms. In the following, two major approaches in jet reconstruction are presented. This entire section is based upon the introductory review 'Towards Jetography' by Gavin P. Salam [Sal10] and a talk given at CERN, [Sal11].

Using an iterative cone (IC) algorithm, a seed particle i above a certain momentum threshold is chosen in order to sum up all particles j that are located within a certain radius R around the seed particle:

$$R_{ij}^2 \;=\; (\phi_i - \phi_j)^2 + (y_i - y_j)^2 < R^2 \tag{1}$$

ϕ is the azimuthal angle and y the rapidity of a particle. The rapidity y is defined as

$$y \;=\; \mathrm{artanh}(\frac{v}{c}) = \frac{1}{2}\ln(\frac{E + p_z}{E - p_z})\,, \tag{2}$$

where c is the speed of light, E the energy of a particle, v its velocity and p_z its momentum in beam direction.

Unlike speeds at relativistic velocities, rapidities are additive quantities. In addition to the rapidity *y*, one also employs the so called pseudorapidity η that takes the place of the polar angle θ with respect to the beam direction. A pseudorapidity of $\eta = 0$ relates to a polar angle of $90°$ (perpendicular to the beam direction), while growing $|\eta|$ tend to a polar angle of $0°$. If the rest mass of a particle is zero or negligible, the pseudorapidity equals the rapidity. That makes the pseudorapidity a suitable quantity for collider physics, as the kinetic energy usually exceeds the rest mass energy significantly. The pseudorapidity is then given by

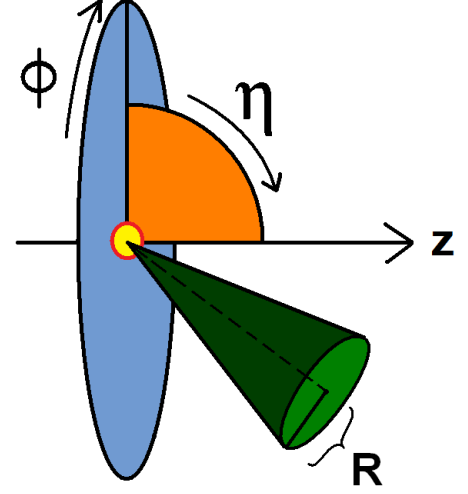$$\eta = -\ln\,\tan\!\left(\frac{\theta}{2}\right). \qquad (3)$$

Figure 1: *Illustration of the quantities ϕ, η and R: Though R is called a radius, it is a dimensionless quantity that defines a cone in the eta phi system with the point of collision as its origin.*

After all particles in the defined cone around the seed particle are allocated, the resulting sum of weighted momenta[1] then serves as the new seed direction. This procedure is iterated until the seed direction stops changing and the stable cone of particles is called a jet.

The question remains which particle qualifies as a seed particle and secondly, how to face the possibility of overlapping cones. A simple way is to choose the particle with the largest p_T as seed particle. This is employed by IC-PR (progressive removal) algorithms which, in a second step, iterate the jet (i.e. a stable cone) and remove all its particles from the event. Because of that every particle can only be assigned to one jet. Although the IC-PR algorithms fix the problem of overlapping cones, they suffer from so called collinear unsafety. Due to a possible, nearly collinear splitting of the hardest particle, the IC-PR approach may misleadingly select seed particles with a lesser p_T which implies a different start direction and a different outcome of jets (illustrated in figure 2).

---

[1]The weight is used to give the correct geometric center of the jet.

There are further cone algorithms that employ the so called split-merge approach that is used upon a set of already stable protojets in order to compute cones that do not overlap. Beginning with the hardest protojet A (largest p_T) the next hardest protojet B that shares particles with A is to be found. If there is no overlap the protojet A becomes an actual jet. Otherwise the total p_T of the shared particles is calculated ($p_{T,\text{shared}}$) in order to determine the ratio $p_{T,\text{shared}}/p_{T,\text{B}}$. If this ratio exceeds a defined limit f, which is called the overlap threshold, both protojets A and B will be replaced with a single merged protojet. Else the protojets are split and the shared particles are assigned according to a certain rule (e.g. assign the shared particles to the protojet with the closest axis).
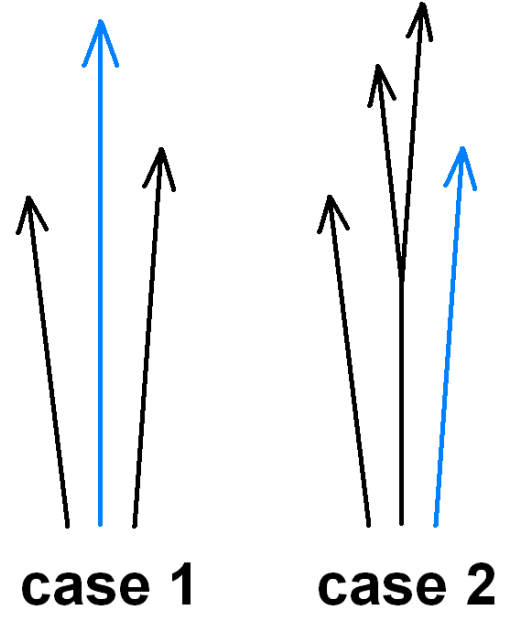

Figure 2: *Collinear unsafety: Due to collinear splitting the hardest particle may vary and the seed particle (blue) changes.*

Since the resulting jets depend on the initial protojets, the outcome of the split-merge approach is sensitive to effects that change the initial set of stable cones, i.e. a randomly occurring soft particle may be considered a seed particle. This problem is called infrared unsafety (illustrated in figure 3). Along with collinear safety, infrared safety is an important property of every algorithm, particularly because the randomly occurring events of collinear splitting and the emission of soft particles are hardly predictable. Beside the IC algorithms there is another major class called sequential recombination algorithms. Main component of these algorithms is always a certain definition of distance between the particles under which a sequential recombination of particles is carried out.
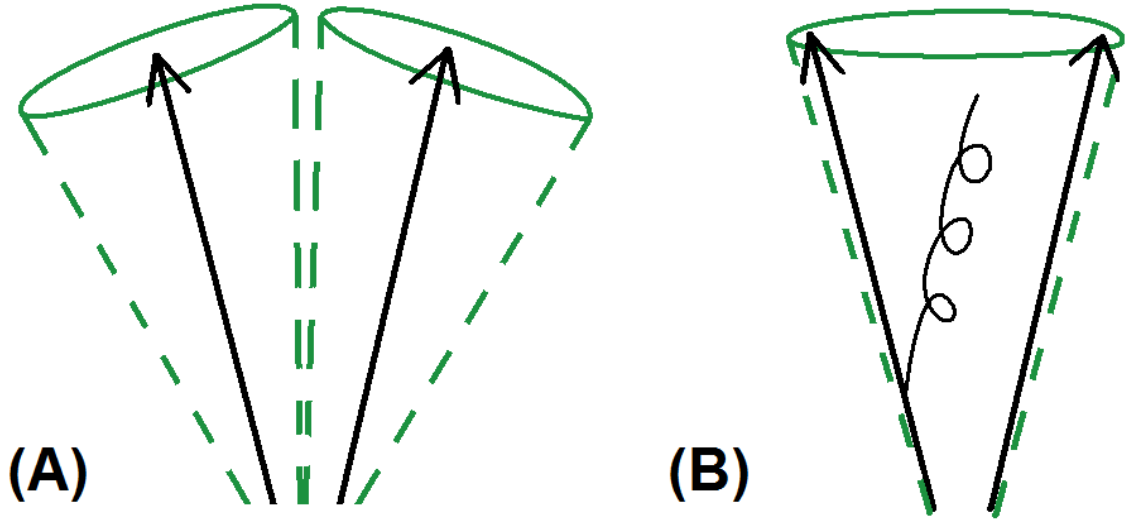
Figure 3: *Infrared Unsafety: Due to a random emission of a soft gluon the set of initial protojets changes which may lead to a different jet.*

In the following three major algorithms will be presented, the Cambridge/Aachen (C/A) algorithm, the k_T algorithm, and the anti-k_T algorithm.

The simplest approach of a sequential recombination of particles is given by the C/A algorithm. It progressively recombines particles that are closest to each other with respect to R_{ij}^2 with a certain R^2 as the limit where a jet is formed. In a generalized way it can be described as follows:

$$d_{ij} = \frac{\Delta R_{ij}^2}{R^2}, \qquad (4)$$

$$d_{iB} = 1 \qquad (5)$$

With the definition of eq. (1), all the distances d_{ij} between the particles i and j are to be computed. The second step is to find out which element of (d_{ij}, d_{iB}) is the smallest. With d_{iB} as the smallest element, the particle i becomes a jet, otherwise the particles i and j will be recombined to a pseudo particle. Thereby all particles will be sequentially clustered in an angular-ordered hierarchy.

The k_t algorithm can be seen as an extension to the C/A algorithm, as it adds the transverse momentum p_T as a second quantity to guide the particle clustering:

$$d_{ij} = \min(p_{T,i}^2, p_{T,j}^2)\frac{\Delta R_{ij}^2}{R^2}, \qquad (6)$$

$$d_{iB} = p_{T,i}^2 \qquad (7)$$

Akin to the C/A algorithm, the k_t algorithm progressively recombines the closest particles with the difference that the distance d_{ij} is now weighted with the smallest transverse momentum of the two particles i and j. As a result soft particles will be primarily recombined and the outcome depends highly on soft particles at the beginning.

Going the other way round, the anti-k_t algorithm prefers a recombination of hard particles:

$$d_{ij} = \min(\frac{1}{p_{T,i}^2}, \frac{1}{p_{T,j}^2})\frac{\Delta R_{ij}^2}{R^2}\ ,\tag{8}$$

$$d_{iB} = \frac{1}{p_{T,i}^2}\tag{9}$$

With these definitions at hand, the cluster grows outwards around the hardest particle. As a consequence, the final jet has a cone-like shape with the initial hardest particle as its virtual seed particle. To conclude this section the jet shapes of some algorithms are displayed in figure 4.
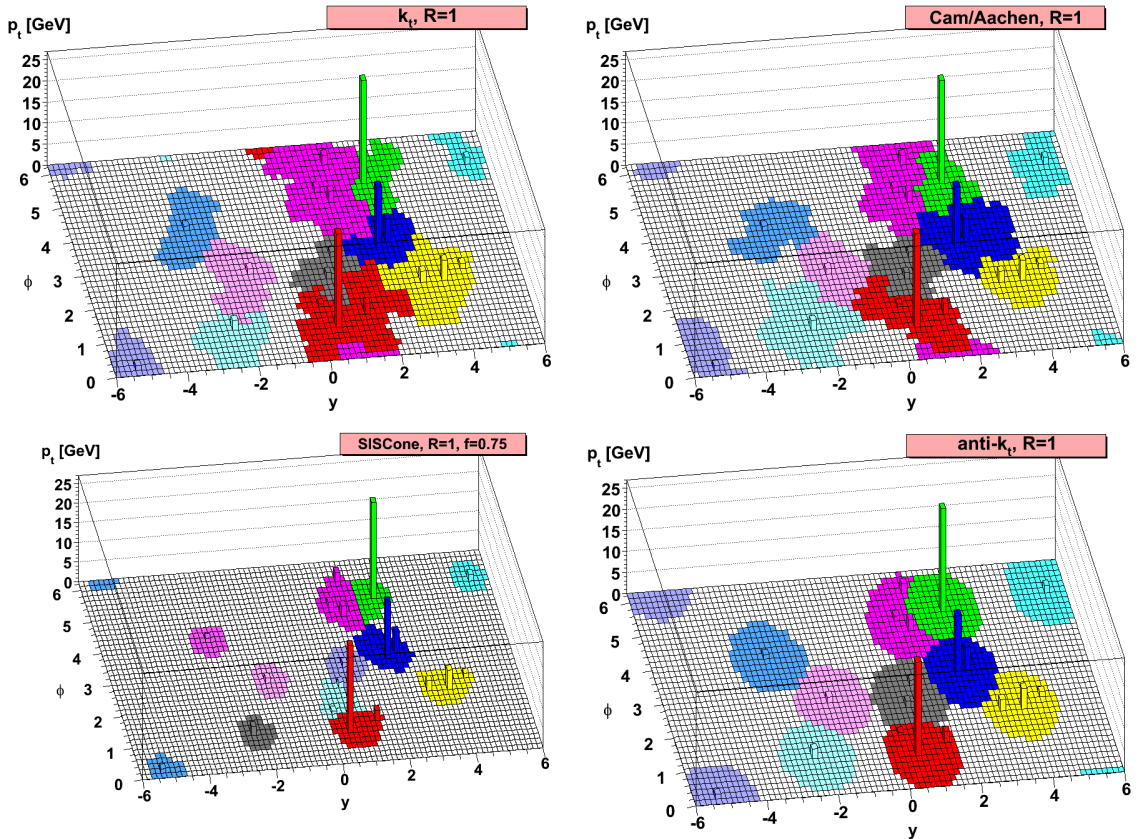

Figure 4: *Shapes of jets from different reconstruction algorithms with respect to the η-φ-plane. Figure taken from [C⁺08].*

2.3 The Glauber Model

In addition to quantities like the momentum and the particle multiplicity, which are directly available by detectors, it is possible to gain access parameters describing the collisions on the microscopic scale. Though it seems impossible to directly retrace the way collisions take place, a method has been developed to look into multiple scattering of nucleons by using experimental data. On the basis of [M$^+$07] it will be explained, how the so called Glauber model is used to gain these insights from collider observations.
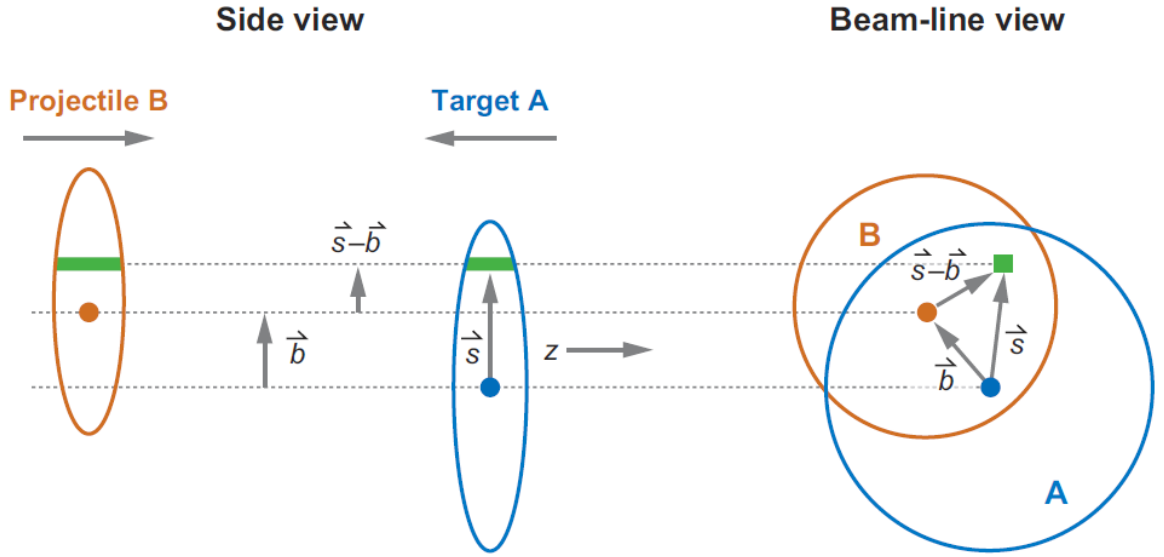
Figure 5: *Schematic Representation of the Glauber model geometry, with a transverse view (left) and a longitudinal view (right). Figure taken from [M$^+$07].*

Given two nuclei and a geometric model to describe the scattering, the Glauber model provides the computation of quantities like the total cross section and the number of participating nucleons as a function of the so called impact parameter b. A geometric model and the definition of the impact parameter b are given by figure 5. The experimental data required for these calculations are the energy dependence of the inelastic nucleon-nucleon cross section and the nuclear charge densities.

Since computational resources are widely available, today's calculations are carried out by a Monte Carlo approach. According to the nuclear densities the nucleons of the participating nuclei are displayed in a three-dimensional coordinate system. The impact parameter b is chosen randomly by the distribution $\mathrm{d}\sigma/\mathrm{d}b = 2\pi b$. The collision of the nuclei is then given by a sequence of binary nucleon-nucleon collisions. With the total inelastic nucleon-nucleon cross section $\sigma_{\mathrm{inel}}^{\mathrm{NN}}$ and the nucleons' distance d in the xy plane, a simple case of a Monte Carlo approach would be provided by the following condition:

$$d \leq \sqrt{\sigma_{\mathrm{inel}}^{\mathrm{NN}}/\pi} \qquad (10)$$

A Monte Carlo event regarding the collision of gold ions at $\sqrt{s_{\mathrm{NN}}} = 200\,\mathrm{GeV}$ is illustrated in figure 6 with an impact parameter of $b = 6\,\mathrm{fm}$. According to (Eq.(10)), the radius r of the nucleons depicted therein is given by

$$r = \sqrt{\sigma_{\mathrm{inel}}^{\mathrm{NN}}/\pi}/2 \ . \qquad (11)$$

The Glauber Monte Carlo approach can deliver distributions as a function of observable parameters like the particle multiplicity.

Figure 6: *A Glauber Monte Carlo event viewed in the transverse xy plane and along the beam axis z. Participating nucleons are drawn in darker colors. Figure taken from [M^{+}07].*

The association to the experimental data is carried out by mapping the Glauber calculation to the corresponding measured distribution. The measured distribution can simply be the per-event particle multiplicity or in the case of the ALICE experiment the counted events as a function of the VZERO amplitude (forward detector amplitude proportional to the multiplicity).[2]

---

[2]For more information about recent Pb-Pb collisions involving Glauber modelling and centrality analysis cf. [A^{+}10].

Figure 7: *Illustrated example of mapping the Glauber calculations to the experimental found distribution. Figure taken from [M⁺07].*

Under the assumption that the impact parameter b is monotonically related to particle multiplicity, both computed and experimental distribution can be subdivided according to the total integral (cf. figure 7). Subsequently, Glauber quantities like the mean number of particles involved $< N_{part} >$ or the mean number of binary nucleon collisions $< N_{coll} >$ can be computed for these centrality divisions and therefore can be associated to the particle multiplicities found in the experiment.

2.4 The Gamma Distribution

The following discussion of the gamma distribution is based on [MT01]. Later on it will be used to parametrize jet spectra.

Given n samples of quantities x_i that were taken from the same probability density function $f(x)$, the probability density function $f_n(x)$ of the random variable S_n with

$$S_n = \sum_{i=1}^{n} x_i \tag{12}$$

is given by the n-fold convolution of $f(x)$:

$$f_n(x) = \int_0^x \mathrm{d}y \, f(y) f_{n-1}(x-y) \tag{13}$$

Regarding independent emission of particles, the quantities x_i and $f(x)$ would be replaced by the random momenta p_i and the inclusive single particle p_T distribution. Introducing the Gamma distribution f_Γ, a probability density function is available that has simple properties under convolution and fits the needs of particle physics:

$$f_\Gamma(x,p,b) = \frac{b}{\Gamma(p)}(bx)^{p-1}e^{-bx}, \tag{14}$$

$$\tag{15}$$

where $x, p, b \in \mathbb{R}_+$ and $\Gamma(p)$ is the Gamma function:

$$\Gamma(p) = \int_0^\infty \mathrm{d}t \, t^{p-1} e^{-t} \tag{16}$$

The gamma distribution is normalized with

$$\int_0^\infty \mathrm{d}x \, f_\Gamma(x,p,b) = 1 \tag{17}$$

The mean μ and standard deviation σ are given by

$$\mu = \frac{p}{b} \, , \, \sigma = \frac{\sqrt{p}}{b} \, . \tag{18}$$

Under a n-fold convolution (Eq.(13)) the parameter b remains unchanged, while p simply varies with $p \rightarrow np$:

$$f_{\Gamma n}(x, p, b) = f_{\Gamma}(x, np, b) = \frac{b}{\Gamma(np)}(bx)^{np-1}e^{-bx} \tag{19}$$

$$\text{with } \mu_n = \frac{np}{b} \text{ , } \sigma_n = \frac{\sqrt{np}}{b} \tag{20}$$

With $p = 2$ the Gamma distribution represents a standard form of the inclusive single particle p_T distribution:

$$\frac{d\rho}{dp_T} = b^2 p_T e^{-bp_T} \tag{21}$$

3 Studying the Quark-Gluon Plasma with ALICE

As one of the major experiments at CERN, the ALICE Experiment has been designed to investigate the physics of heavy-ion collisions. Working with Pb-Pb collisions at a centre of mass energy of more than 2 TeV per nucleon pair, it is possible to study the properties of the so called quark-gluon plasma (QGP), a phase where gluons and quarks are no longer confined.

While the QGP itself only exists for a short time, its effects become visible by the phenomenon called 'jet quenching'. The term refers to the suppression of jets with high momentum by interaction with the QGP. As jets of high momentum usually arise from two partons, that were scattered back to back, the spectrum of the transverse jet momentum can be used to quantify the influence of the QGP. In case of jets being formed at the edge of the QGP volume this effect becomes most striking, as one jet will escape the QGP without interaction while the second jet may travel through the whole distance of the QGP. To analyse the collisions ALICE is equipped with several detectors. The information presented here is taken from [GO09].

- The Inner Tracking System (ITS) consists of six cylindric silicon detectors in order to locate the point where emerging particles originate, accordingly called the primary vertex.

- The Time Projection Chamber (TPC) is used to trace the route of particles. Passing through the gas in the chamber, the particles leave a path of ionized molecules.

- The Photon Spectrometer (PHOS) is a calorimeter which is used to measure photons. As a result particles like π^0 can be identified by their decay photons.

- Crossing the interface of media of different dielectric constant, charged particles of high energy emit transition radiation. The Transition Radiation Detector (TRD) uses this effect for its main task discriminating electrons from hadrons.

- The Time-of-Flight Detector (TOF) features so called Multigap Resistive Plate Chambers (MRPC) in order to identify charged particles.

- In addition to the PHOS, the ElectroMagnetic Calorimeter (EMCal) is employed to detect photons as well as neutral mesons in a wider range of acceptance, but with a worse energy resolution and smaller granularity.

- The High-Momentum Particle Identification Detector (HMPID) is a Ring-Imaging Cherenkov detector (RICH) measuring the velocity of hadrons that are too fast to be detected by the ITS, the TPC or the TOF.

The following schematic view illustrates the setup of ALICE (figure 8).
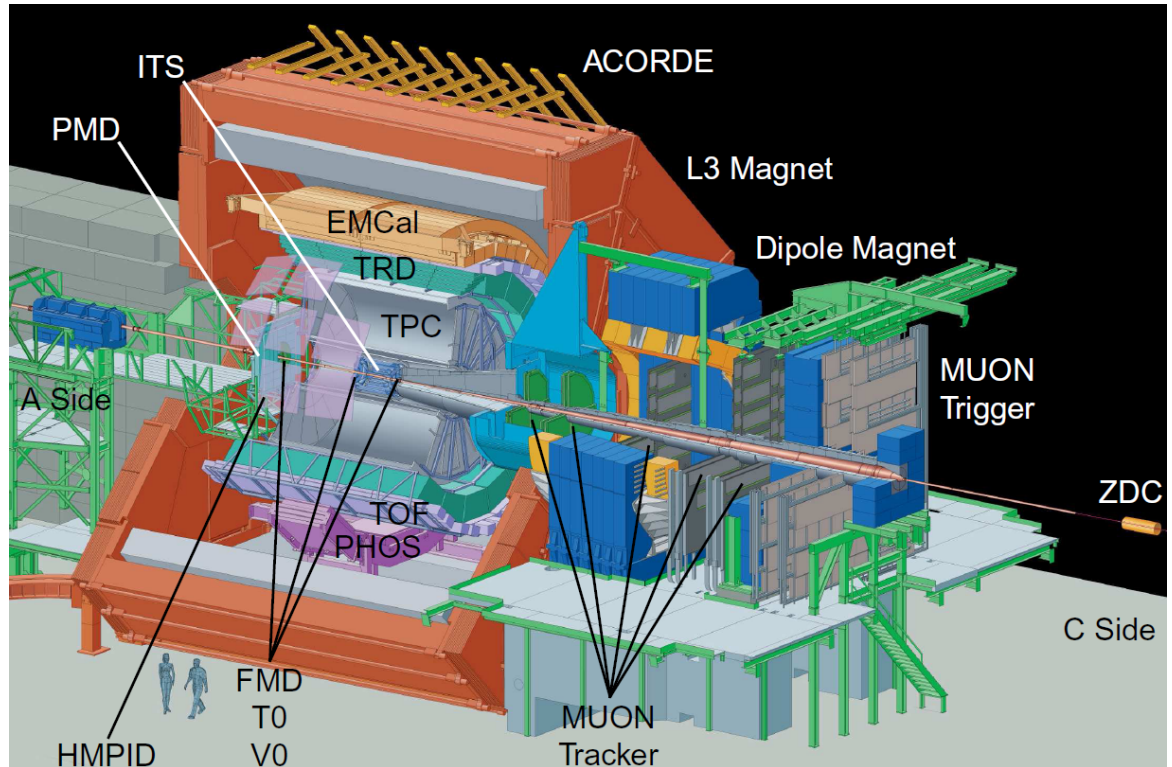
Figure 8: *Schematic View of the ALICE experiment. Figure taken from [GO09].*

4 Studying Background Fluctuations

The first Pb-Pb collisions took place at CERN in fall 2010. The observations showed a striking dijet-imbalance [A$^+$10] which seems to be powerful evidence for the existence of medium-induced jet quenching (figure 9). Nevertheless a quantitative analysis of possible effects must precede any significant quantification of medium-induced effects. Therefore it is still to examine what these imbalances are caused by in detail which demands an analysis of the background influence.

Figure 9: *Jet-quenching: The figure shows the η-ϕ-plane and the transverse momentum of two particle jets emerging from a Pb-Pb collision recorded at the CMS Experiment at CERN. Although the two jets point in opposite directions, their transverse momentum varies. Figure taken from a talk held at CERN, [Oet11].*

In the following the current efforts on this issue are portrayed briefly based on [KB11]. The underlying data of tracks were provided by charged particles tr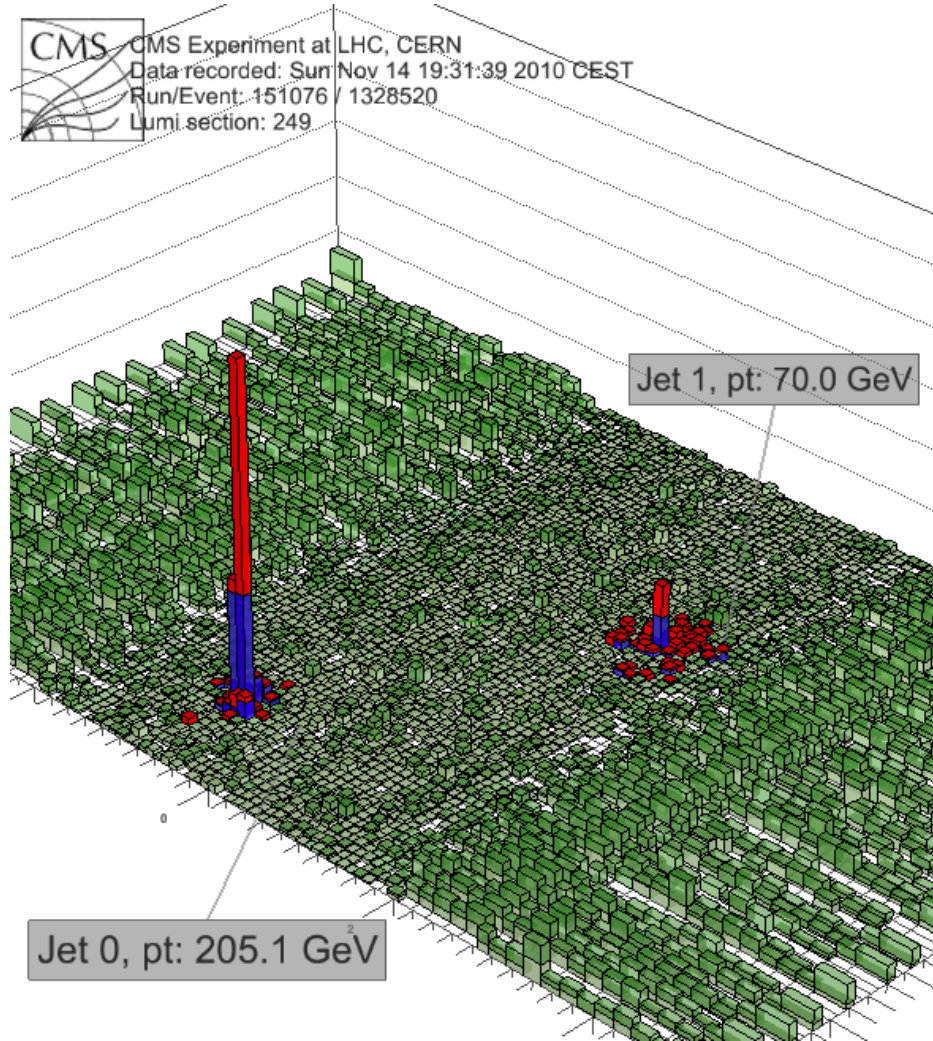aced in the TPC and by additional vertexing information of the ITS. In an attempt to estimate the influence of the background, the background density ρ was estimated by calculating the median p_T per area of reconstructed k_t-clusters after removing two leading jets. Using anti-k_t clustering with subtracting the background for the jet area A in each event, i.e.

$$p_T^{\text{rawjet}} = p_t^{\text{cluster}} - \rho \cdot A \,, \tag{22}$$

the raw jet spectra could be obtained.
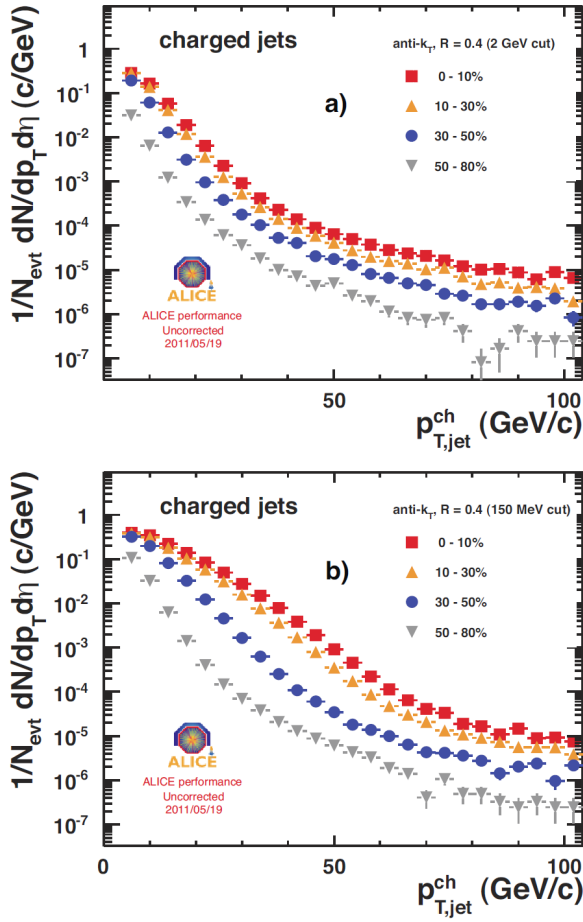
Figure 10: *Raw jet spectra for different centralities after background subtraction: a) p_T cut of 2 GeV, b) p_T cut of 150 MeV. Figure taken from [KB11].*

The results depicted in figure 10 feature evidence of background fluctuations as the spectra vary for different centralities. These residuals were obtained using a track p_T cut of 2 GeV. A lower cut of 150 MeV resulted in an even clearer difference.

One attempt to examine the fluctuations was to place random cones into the jet acceptance summing the momenta of all tracks. Subsequently, the background was subtracted in order to get the residuals δp_T:

$$\delta p_T = p_t^{\text{cone}} - \rho \cdot A \tag{23}$$

Background residuals were also computed for randomized events in η and ϕ thus annihilating regional correlations. As a result the residuals were reduced to purely statistical fluctuations (cf. figure 11a)).
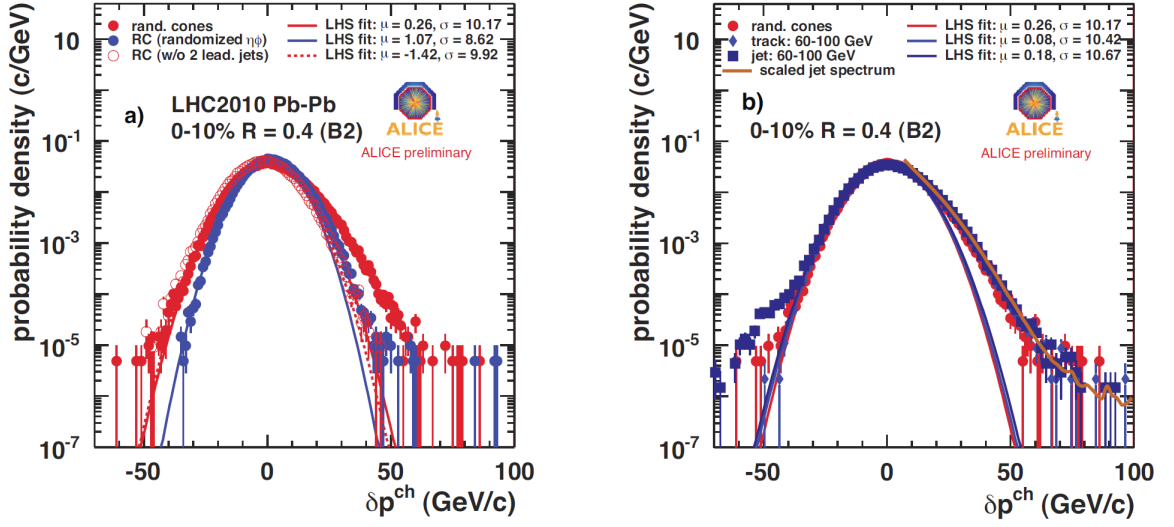
Figure 11: *a) δp_T distribution in the 10 % most central Pb-Pb events for random cones on full events, on randomized events and excluding a certain area of the two leading jets. The latter only influences the right-hand side (high p_T) as expected. b) δp_T distribution in the 10 % most central Pb-Pb events for different probes together with scaled jet spectrum and p_T cut of 150 MeV. Figure taken from [KB11].*

To examine the background induced influence on jet reconstruction, full pp jet events and single high p_T tracks have been embedded to act as virtual seeds for a subsequent anti-k_t clustering. The use of the anti-k_t algorithm implies circular clustering and thus, results similar to random cones (cf. figure 11b)) with the difference that it now provides information on the background influence on actual jet reconstruction. After subtracting the background and the embedded probe with, the residuals δp_T are given by

$$\delta p_T \;=\; p_T^{\text{cluster}} - \rho \cdot A - p_T^{\text{probe}} \;. \tag{24}$$

The background residuals that has been obtained by embedding high p_T tracks represent the data used in the following analysis.

5 The Parametrization of Jet-Induced Background Fluctuations

In the last section it has been shown that the distributions of background residuals δp_T consist of a part that is purely statistical and a part that is caused by fluctuations of different nature, both for random cones and embedding. In the following analysis, the δp_T distributions will be parametrized with respect to the purely statistical part and the jet-induced fluctuations. The underlying data was gained from embedding of high-p_T tracks and anti-k_t clustering with a distance factor $D = 0.4$ and a track p_T cut of 150 MeV (cf. previous section). The complete data of the parametrization can be found in the appendix. In the following analysis, the quantity χ^2/NDF always considers the points within the respective fit range only.

5.1 Preparation of Background Residuals of Statistically Independent Emission

Only with a description of the statistical part of the background residuals the analysis of experimental data can lead to significant knowledge about the fraction that is jet-induced. Therefore it is recommended to start with residual distributions of statistically independent δp_T. This will be achieved by randomly adding up single particle p_T that will thus lead to a spectrum of statistically independent emission followed by a correction for the mean background density similar to (Eq.(23)). In addition, a distinction between multiplicity classes will be made. Below, the way the distributions are simulated is explained.

- At first, a mean background B per jet area πR^2 for a multiplicity m is computed with

$$B \;=\; <p_T> \cdot m \cdot \frac{\pi R^2}{2\pi \eta_{\text{ac}}} \tag{25}$$

$$\;=\; <p_T> \cdot m \cdot \frac{0.4^2}{3.6} \;, \tag{26}$$

  where $<p_T>$ is the mean momentum taken from the spectrum of single tracks (with the p_T cut at 150 MeV) and $2\pi\eta_{\text{ac}}$ an adjustment for the given track acceptance $\eta_{\text{ac}} = 2 \cdot |\eta| = 1.8$. The value of R is the radius resulting from anti-k_t 'cones' $D = 0.4$.

- In order to get the momentum p_T - virtually reconstructed in the given jet area - random momenta from the single track spectrum are summed. The number of summands is given by the multiplicity per jet area $m \cdot 0.4^2/3.6$ (similar to B).

- Then the background residuals δp_T are

$$\delta p_T \;=\; p_T - B \tag{27}$$

- The computation are carried out for a large amount of multiplicities $m \in \,]0, 3400[$. The m therein are chosen from the multiplicity distribution found in experimental data.

- Finally, the $\delta p_T(m)$ are divided into 17 classes of multiplicity M with $M = 0$ for $m \in [0, 199]$, $M = 1$ for $m \in [200, 399]$ and so on. The result can be seen in figure 12.
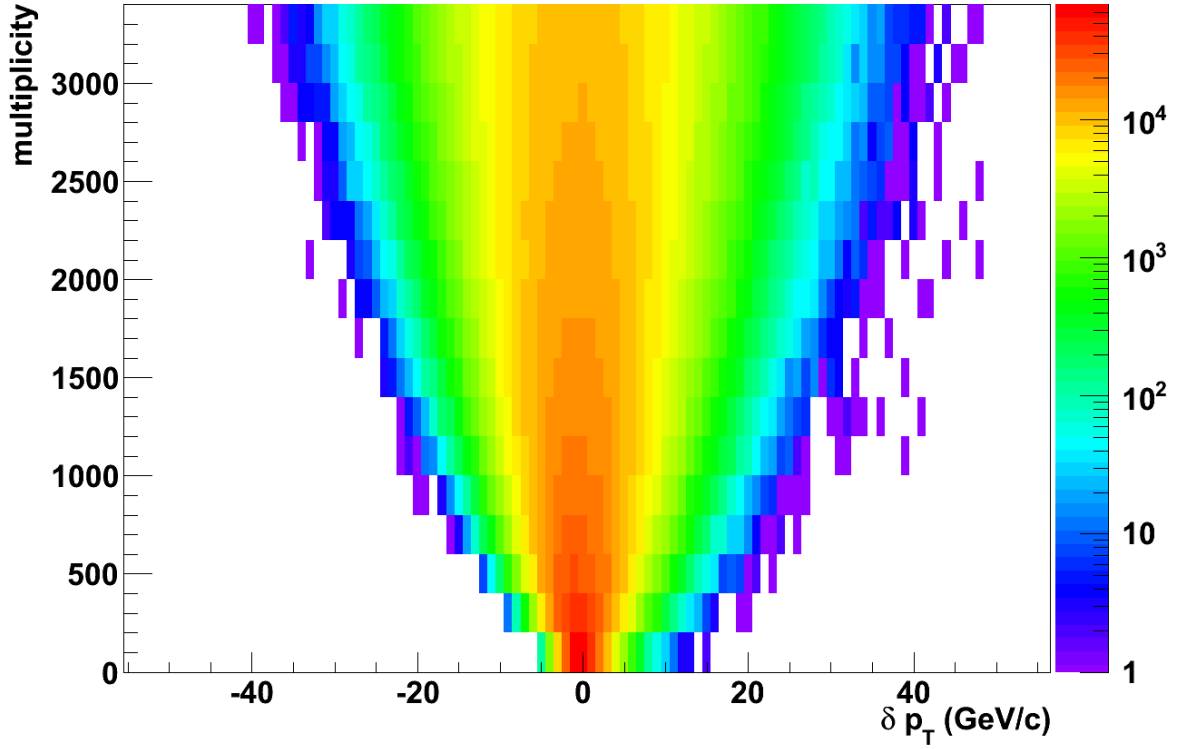

Figure 12: *The simulated δp_T spectrum as a function of the multiplicity. The y-axis is subdivided into 17 classes of multiplicity.*

For the upcoming parametrization the spectra were normalized. Therefore they can be seen as probability densities of background residuals following statistically independent emission.

5.2 Parametrization of Background Residuals of Statistically Independent Emission

In order to parametrize the distributions of independent emission the Gamma distribution (Eq.(15)) will be used. Additionally, a simple proportionality factor a is appended and the mean $\mu = p/b$ (Eq.(18)) is subtracted for the distribution to be peaked around zero:

$$a \cdot f(p, b, \delta p_T + \frac{p}{b}) = g(p, b, \delta p_T, a) = \frac{ab}{\Gamma(p)} \left[b(\delta p_T + \frac{p}{b}) \right]^{p-1} e^{-b(\delta p_T + \frac{p}{b})} \qquad (28)$$
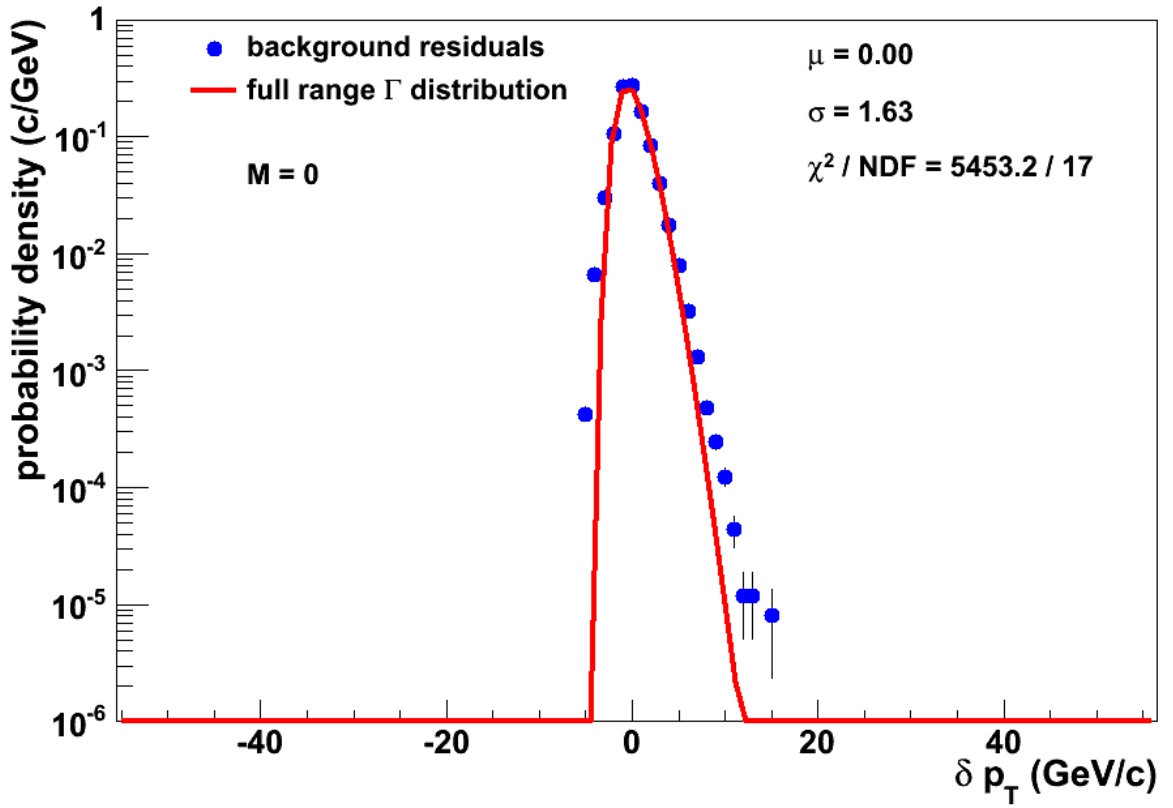
Figure 13: *Illustration of the Gamma distribution fitted to the residual spectrum for the multiplicity class $M = 0$. Denoted are the mean μ and the standard deviation σ of the residual distribution and the χ^2/NDF of the fit.*

Though the fit of the Gamma distribution was computed for the whole range, it does not work well for the smallest multiplicity class $M = 0$ with $\chi^2/NDF \approx 321$ due to a low number of supporting points (cf. figure 13). For $M = 1$ the fit has improved with $\chi^2/NDF \approx 7$ and for the rest of the classes χ^2/NDF only ranges from 0.67 to 1.49.

Characterization of Heavy-Ion-Background in Jet-Reconstruction 21
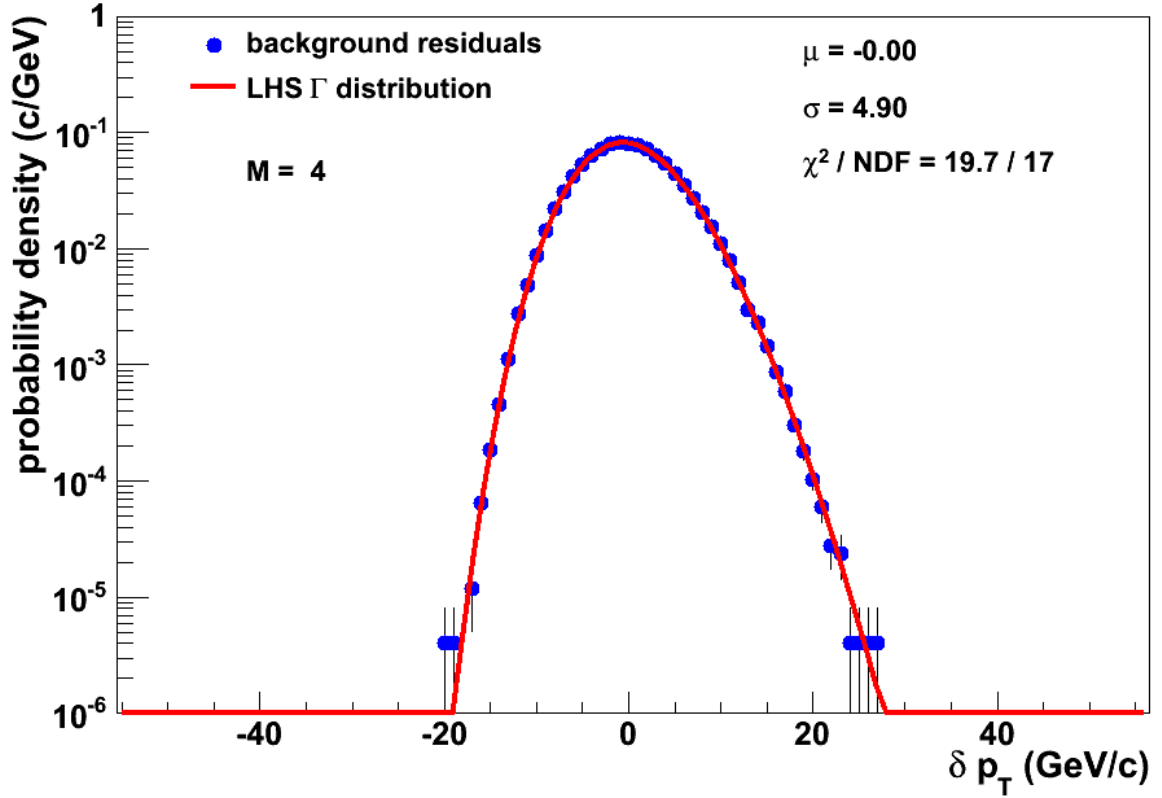
Figure 14: *Illustration of the Gamma distribution fitted to the left-hand side* $[-70,0]$ *of the residual spectrum for the multiplicity class M = 4. Denoted are the mean* μ *and the standard deviation* σ *of the residual distribution and the* χ^2/NDF *of the fit.*

The question of interest is now whether the fit works equally well with the fit range limited to the left-hand side ($[-70,0]$) (e.g. cf. figure 14). This would qualify the Gamma distribution for a parametrization of background residuals given by high-p_T track embedding. This is because jet-induced fluctuations are of positive energy and thus only affect the right-hand side of the residual spectrum.

Now the parameters p, b, p/b, a from (Eq.(28)) will be discussed, i.e. how they vary for both cases of full range and left-hand side fit. As the fit procedure failed for multiplicity class 0 and 1 for both fit ranges, these classes are ignored in the following analysis. The uncertainties of the parameters p, b, a are given by the fit procedure. For now the assumption is made that p and b are independent parameters. Therefore the uncertainty of p/b is given by

$$\Delta(\frac{p}{b}) = \sqrt{(\frac{1}{b}\Delta p)^2 + (\frac{p}{b^2}\Delta b)^2} \tag{29}$$

In figure 15 the relation between multiplicity class M and parameter p is displayed. Because

the parameter p is believed to be proportional to the multiplicity (cf. section 2.4), a line of best fit was plotted with

$$p(M) = \alpha(M + \frac{1}{2}) + \beta \tag{30}$$

$$\text{with } p(-\frac{1}{2}) = 0 + \beta , \tag{31}$$

since a multiplicity of zero and therefore $p = 0$ is approximately found at $M = -1/2$. Therefore the constant β reflects a displacement from the expected case.

Figure 15: *Parameter p as a function of multiplicity class M for a) a full range fit and b) a left-hand side fit of the Gamma distribution. In each case the line of best fit (eq.(31)) was plotted. Denoted are the parameters and the χ^2/NDF of the fit.*

The linear correlation between p and the multiplicity m is reproduced for the left-hand side fit of the Gamma distribution (cf. figure 15b). The uncertainties Δp gained from the left-hand side fit have almost been doubled. A further noticeable difference is represented by the constant β and the slope α. While the β of the full range fit is about zero, the β of the left-hand side fit points to a displacement of $\delta M \approx -1$. In conjunction with this displacement, the slope α differs with approx. 14 %.

Figure 16: *Parameter b as a function of multiplicity class M for a) a full range fit and b) a left-hand side fit of the Gamma distribution. In each case a constant fit was plotted. Denoted are the mean of b and the χ^2/NDF of the fit.*

Figure (16) shows that b is constant which is just as expected as b should be constant under convolution and thus constant for every m. As for the parameter p the uncertainty Δb increases notably for the left-hand side fit. The mean $<b>$ of both cases only differ slightly (approx. 1 %).

Figure 17: *The fraction p/b as a function of multiplicity class M for a) a full range fit and b) a left-hand side fit of the Gamma distribution. In each case the line of best fit (eq.(31)) was plotted. Denoted are the parameters and the χ^2/NDF of the fit.*

With b constant the fraction p/b follows the linear shape of p (cf. figure 17). It might have been seen for p and b that they generally share the same fluctuations, i.e. p and b are dependent parameters to some extend. That observation is equivalent to the fact that the uncertainties $\Delta(\frac{p}{b})$ are estimated too large which can be seen by a strikingly low $\chi^2/NDF \approx 0,2$ for both cases. Accordingly, p/b provides a more stable parameter with respect to the left-hand side fitting of the Gamma distribution. Emphasizing this observation, the slope α and the constant β of both cases only differ within their uncertainties.[3]

Finally, with the simple proportionality factor a being constant at about 1 the validity of the Gamma distribution for both fit ranges is once more approved (cf. figure 18).

---

[3]While working out the fit of the Gamma distribution, it has been noticed that there were often pairs of abnormally high or low p and b preferred by the fit algorithm. The resulting fits seemed appropriate with respect to the χ^2/NDF, but the relative uncertainties of p and b provided by the fit have always been suspiciously large. Nevertheless, the fraction p/b in these cases already proved stable on a low degree.
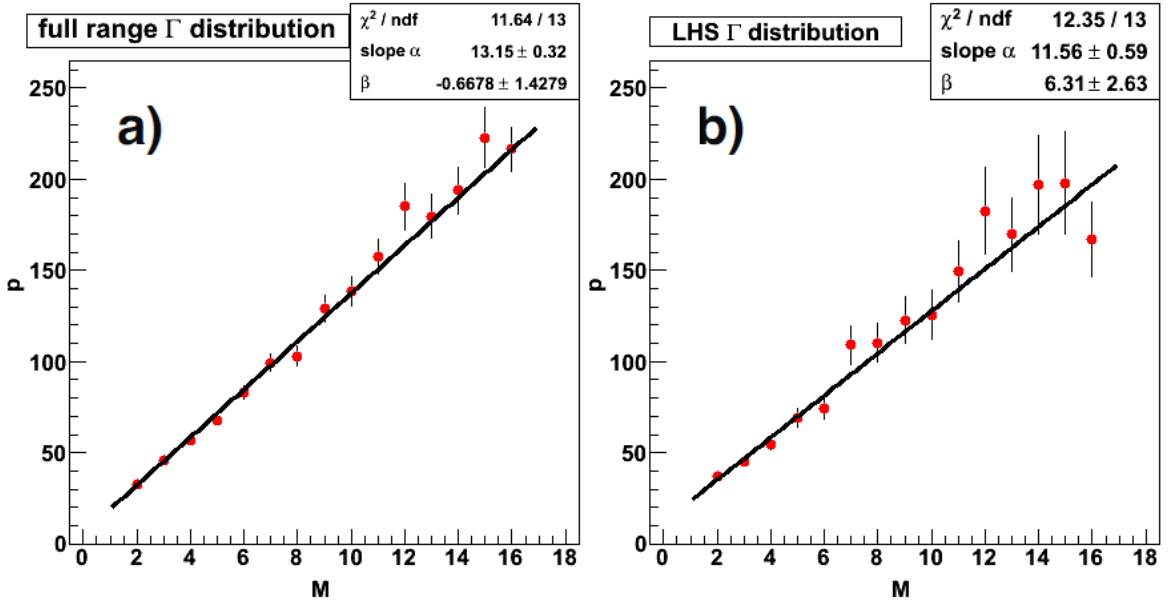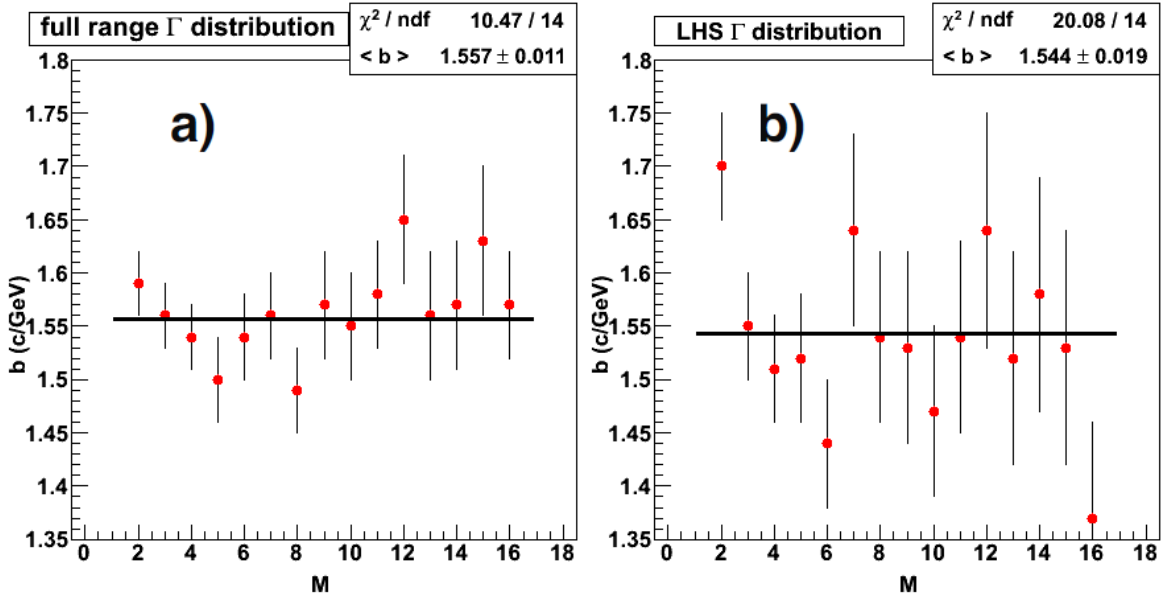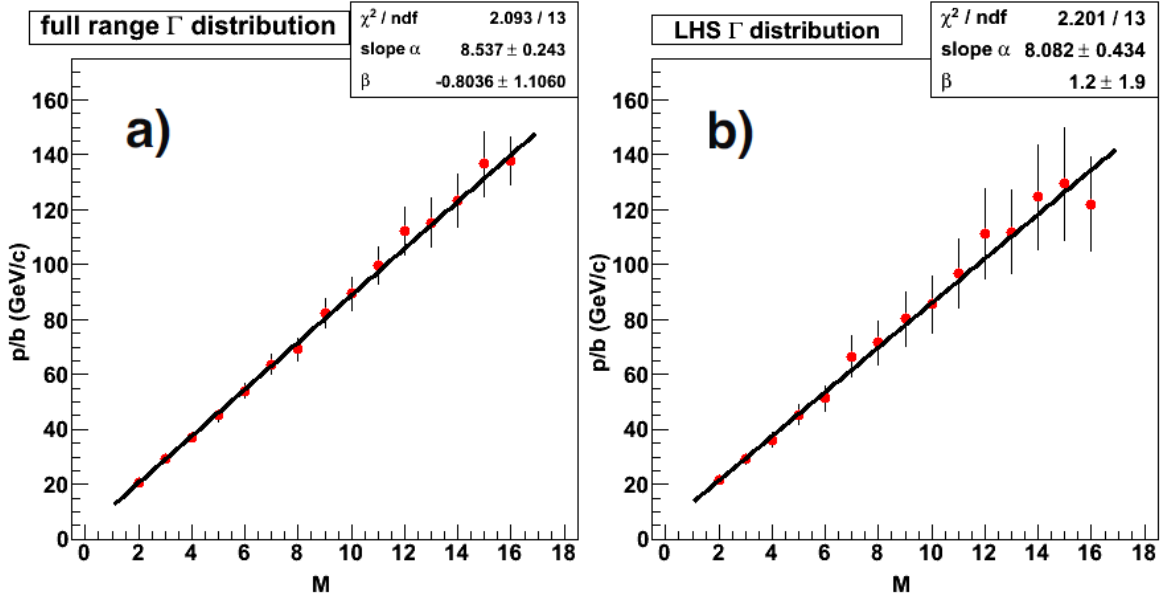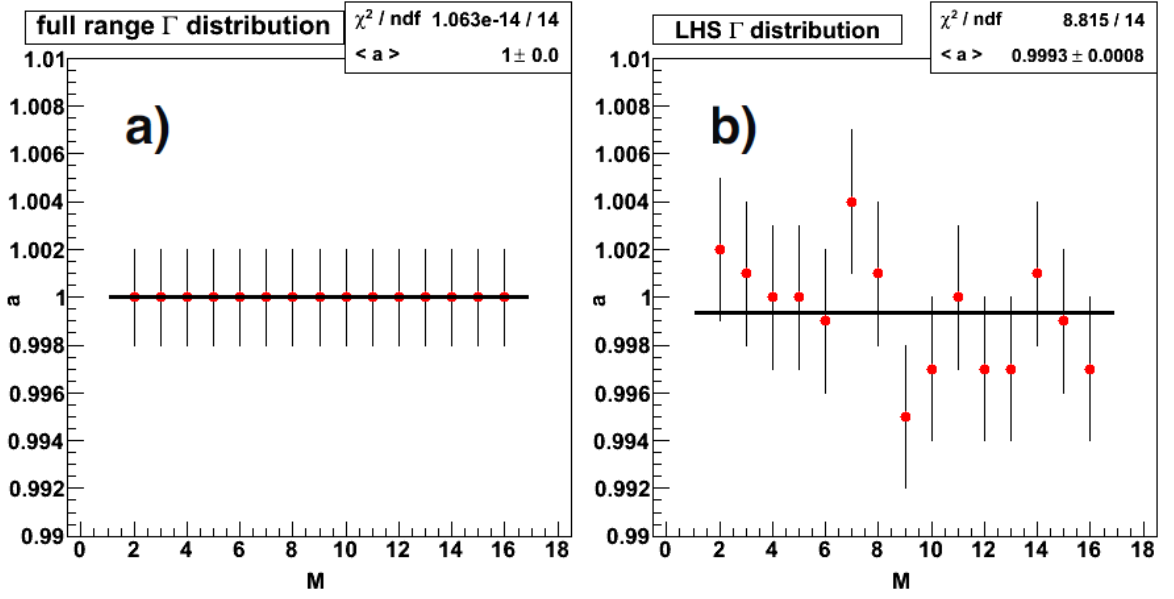
Figure 18: *Parameter a as a function of multiplicity class M for a) a full range fit and b) a left-hand side fit of the Gamma distribution. In each case a constant fit was plotted. Denoted are the mean of a and the χ^2/NDF of the fit.*

In this section it has been shown that the Gamma distribution describes the simulated spectrum of independent emission. This is no trivial finding, because the underlying single track spectrum in truncated with a p_T cut of 150 MeV. Issues like a uneven detector efficiency may have influence. Moreover, the fraction of the single track spectrum with the highest p_T is described by Rutherford parton scattering, which is ignored herein.

Another important result of this section is the proof that a left-hand side fit of the Gamma distribution describes the spectrum almost as well, especially with respect to the parameter p/b.

5.2.1 Mean Momentum and p/b

When the Gamma distribution was introduced in section 2.4, it has been pointed out that the fraction p/b provides the mean of the distribution. Specifically, the mean of the inclusive single track spectrum can be derived from p/b. Since the used single track spectrum has a p_T cut of 150 MeV, the relation $p/b = <p_t>$ is yet to be examined. For that purpose the parameter p/b will be compared to B, which is the $<p_T>$ multiplied with the multiplicity and adjusted for the track acceptance and clustering area (B already had been introduced in equation (5.1)).
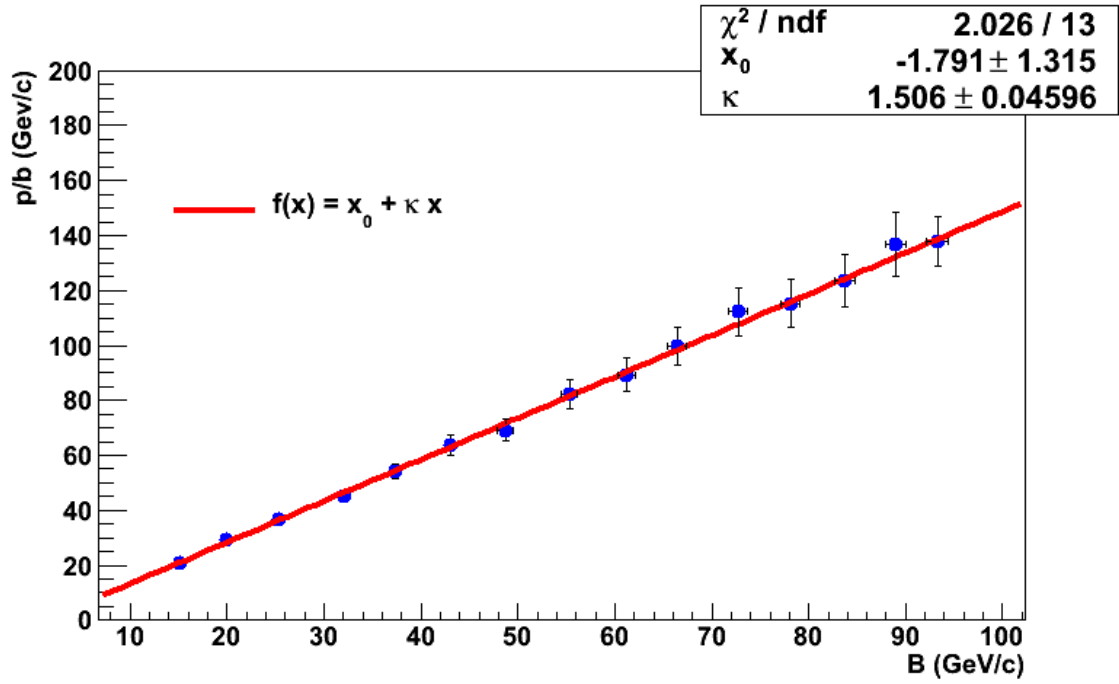
Figure 19: *Correlation of p/b and B. Denoted are the parameters and the χ^2/NDF of the fit function.*

In figure 19 p/b is plotted against B for the given multiplicity classes.[4] The ratio of both is not unity, as it would be expected for a non-truncated single particle track spectrum. Nevertheless, with the slope $\kappa = 1.51 \pm 0.05$ a correction factor is given. Divided by the multiplicity m and with undoing the adjustment for the track acceptance and clustering area, $p/b \cdot \kappa$ should provide the $< p_T >$ of the single track spectrum:

$$< p_T >_{p/b} = \frac{p}{b} \cdot \frac{1}{\kappa} \cdot \frac{1}{m} \cdot \frac{2\pi\eta_{ac}}{\pi R^2} \tag{32}$$

E.g. with $M = 9$ with $m \approx 1900$ the resulting $< p_T >_{p/b} = 0.65 \, \text{GeV/c} \pm 0.05 \, \text{GeV/c}$[5] matches the mean momentum of the single tracks $< p_T > = 0.65 \, \text{GeV/c} \pm 0.44 \, \text{GeV/c}$. Thereby, the parameter p/b with the factor κ remains a valid expression for the mean momentum.

---

[4]Like for p/b in figure 17, the χ^2/NDF seems again too low with approx. 0.15. It is to recall that the uncertainty was estimated too high due to the dependency of p and b.

[5]The uncertainty of $< p_T >_{p/b}$ was estimated with the uncertainty of p/b.

5.3 Parametrization of Experimental Data

It has been shown that the Gamma distribution can describe the full spectrum when only fitting the left-hand side. It will now be used for parameterizing the contribution of jet-induced background residuals on the right-hand side which will be carried out in two ways. At first, it will be examined how the assumed purely statistical part relates to the jet-induced effects by finding a correction function. The second approach consists of simply fitting the Gamma distribution to the right-hand side of the experimentally found residuals. If the fit procedure worked for that case, the jet-induced effects could be parametrized by the Gamma distribution parameters.

5.3.1 Parametrization via Correction Function

The left-hand side fit of the Gamma distribution to the experimental data shows a pronounced deviation of the right-hand side (e.g. cf. figure 20).
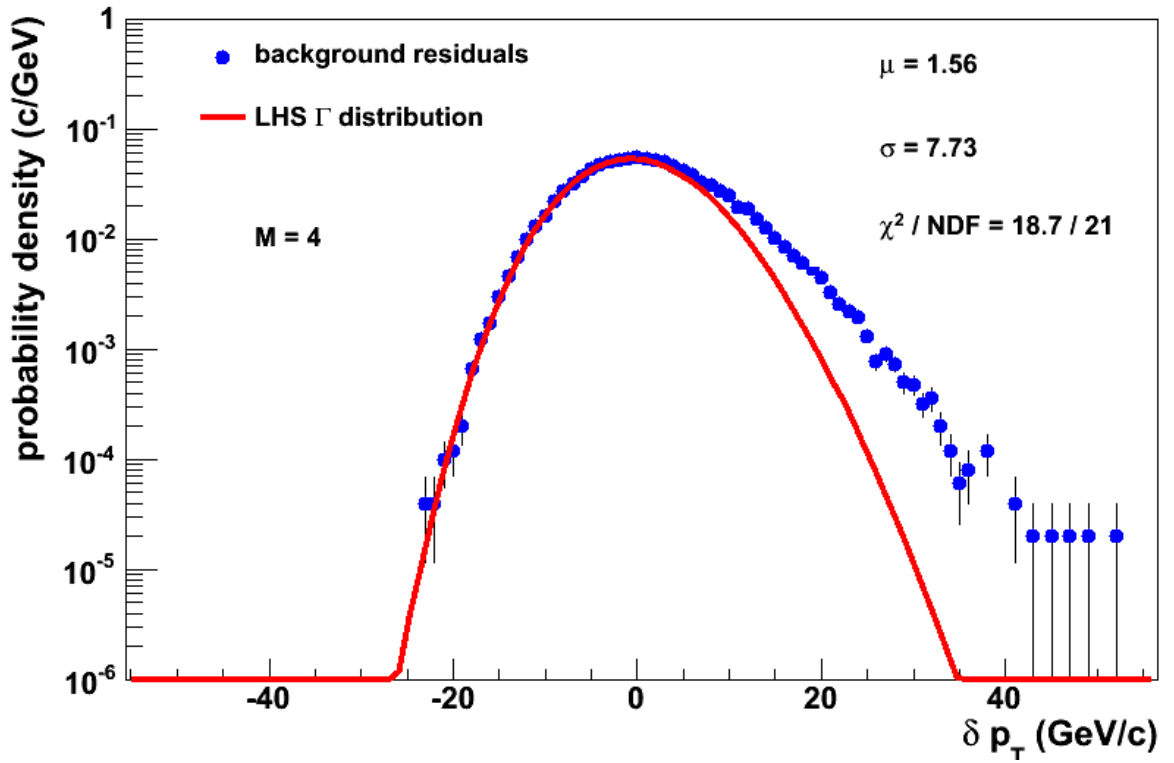
Figure 20: *Illustration of the Gamma distribution fitted to the left-hand side of the background residuals that have been found experimentally for the multiplicity class $M = 4$. Denoted are the mean μ and the standard deviation σ of the residual distribution and the χ^2/NDF of the fit.*

Ideally, the fit function should match the fit function found for the simulated case of

independent emission. However, the fit procedure has been more complicated in this case. The parameter b had to be fixed with $b = 1.55\,\text{c}/\text{GeV}$, because the pairs of p and b proved very unstable during the fit procedure. That way a adequate fit of the left-hand side could be achieved with a χ^2/NDF of 0.81 to 1.36 for the multiplicity classes $M \geq 3$. The complications suggest that the left-hand side itself does not meet purely statistical properties. In fact, the found parameters differ from the parameters found for independent emission. The proportionality factor a no longer is unity, but over 10 % lower for every multiplicity. Additionally, the fraction p/b and is over 50% larger now. This may point to additional non statistical fluctuations, e.g. caused by elliptic flow. The term refers to collective effects that can be estimated quantitatively with a hydrodynamic model [?]. A recent article about the elliptic flow in Pb-Pb collisions is given by [?]. Nevertheless, the disturbance is assumed small in comparison with the jet-induced contribution on the right-hand side.
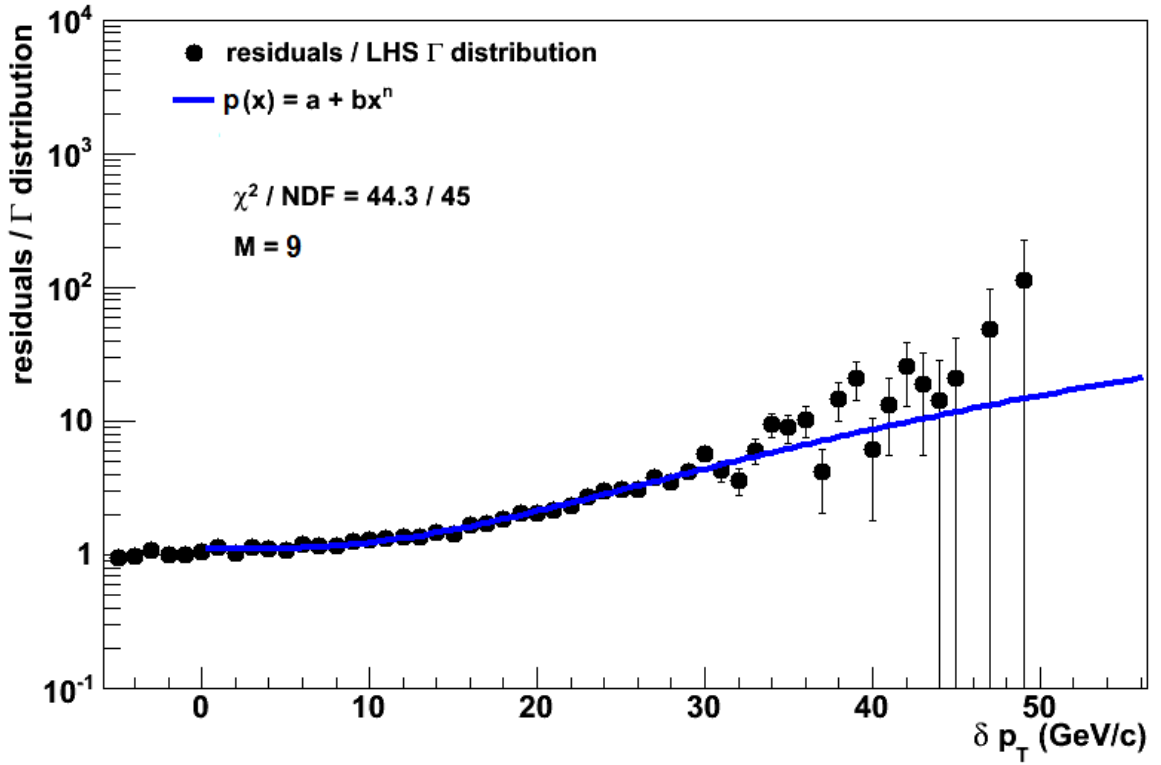
Figure 21: *Illustrated is the ratio between the background residual spectrum and the values expected by the Gamma distribution. A fit of the function $p(x)$ was plotted accordingly.*

A first attempt to quantify the ratio of the fit and the given residuals was made by

defining the power law function $p(x)$:

$$p(x) = a + bx^n ,\tag{33}$$

where the coefficient b is not to be mistaken with the Gamma distribution parameter. An example for $M = 9$ is presented in figure 21. Unfortunately $p(x)$ does not work well for low multiplicity classes $M \leq 7$ and the parameter b seems unstable and afflicted with a high uncertainty for all M.
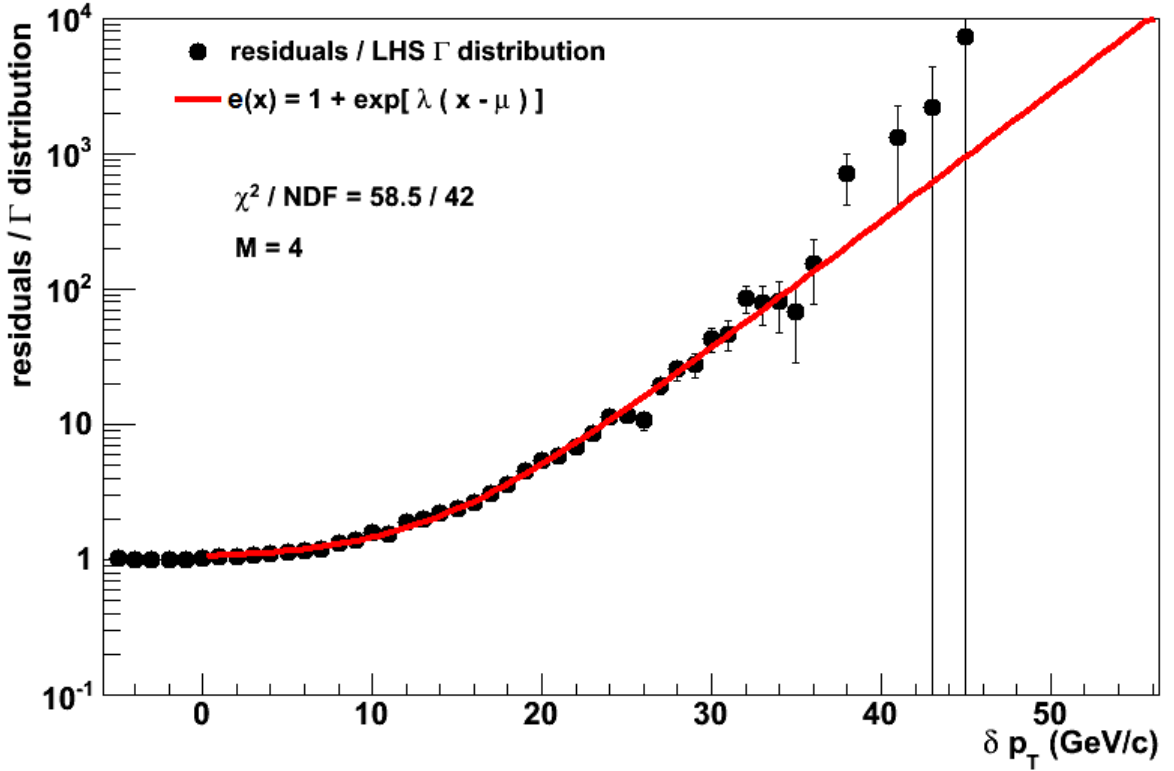
Figure 22: *Illustrated is the ratio between the background residual spectrum and the values expected by the Gamma distribution. A fit of the function $e(x)$ was plotted accordingly.*

A second approach is now given by an exponential function with two parameters:

$$e(x) = 1 + \exp\left[\lambda(x - \mu)\right]\tag{34}$$

This function describes the ratio of residuals to Gamma distribution quite well, as the χ^2/NDF ranges from 0.7 to 2.1 for all multiplicity classes. Equally important, the parameters λ and μ are stable with a relative error less than 4 % for almost all cases. In figure 23 and 24 the behavior of the parameters depending on the multiplicity is depicted. The

multiplicity classes $0, 1, 2$ will be ignored, since the Gamma distribution fit failed for these classes ($\chi^2/\text{NDF} \geq 4$).
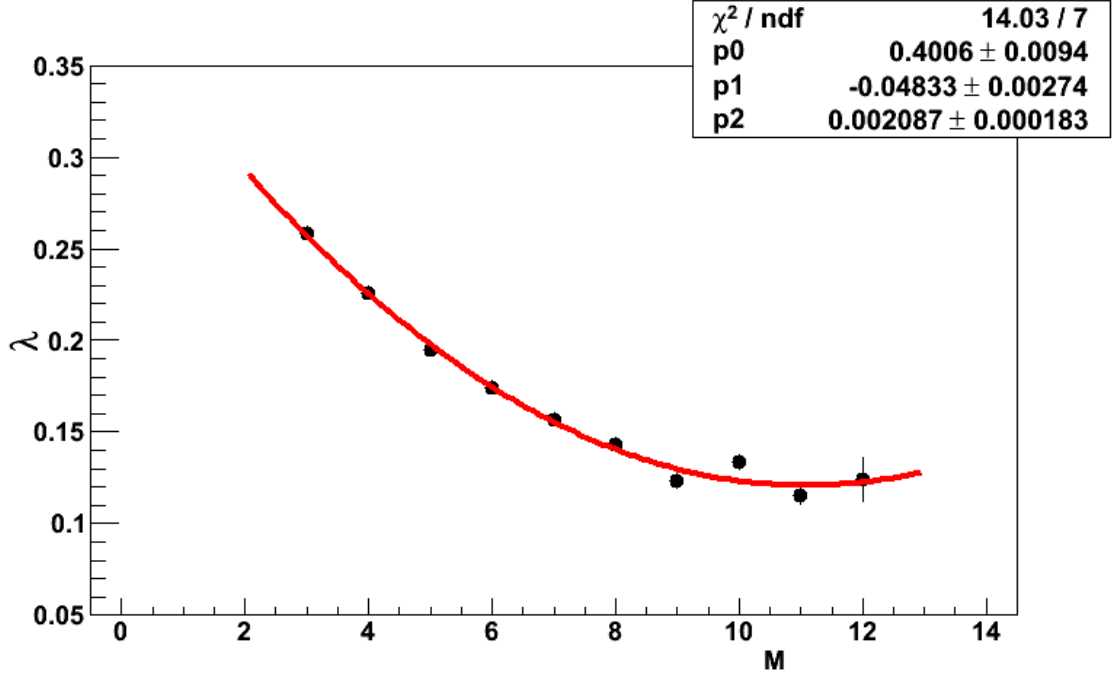
Figure 23: *In this graph it is depicted how the parameter λ of function $e(x)$ (Eq.(34)) evolves for different multiplicity classes M. A second order polynomial fit (Eq.(35)) has been plotted in addition.*

After the function $e(x)$ (Eq.(34)) has proven useful to parametrize the ratio of background residuals and the gamma distribution, the parameters of $e(x)$ themselves are examined. It would be an useful feature, if the parameters followed a simple function. For this purpose a second order polynomial fit $p_2(x)$ with

$$p_2(x) = p_0 + p_1(x + \frac{1}{2}) + p_2(x + \frac{1}{2})^2 \tag{35}$$

has been plotted as it can be seen in figure 23 and 24: As the underlying data is too few, this issue will not longer be pursued in this analysis. Nevertheless, the plots gives a first impression of a possible pattern the parameters may follow. An appropriate function would make the parametrizing function $e(x)$ a function of the multiplicity only.
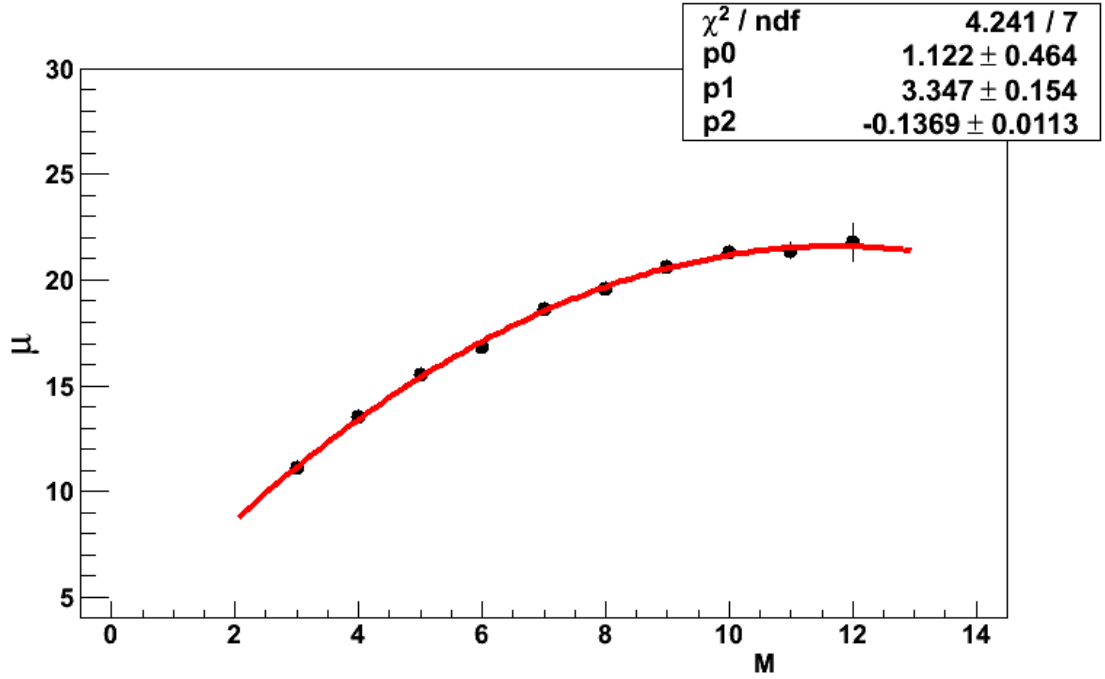
Figure 24: *In this graph the evolution of the parameter μ of function e(x) (Eq.(34)) is shown for different multiplicity classes M. A second order polynomial fit (Eq.(35)) has been plotted in addition.*

In this section, a power law function and a exponential function with two parameters have been tested to describe the ratio between the jet-induced part of the background residual spectrum and the Gamma distribution which is assumed to only describe the purely statistical part. The exponential function has proven better with respect to the overall χ^2/NDF and stability of its parameters. The data that parametrizes the given experimental data via the exponential function can be found in the appendix.

5.3.2 Parametrization via Gamma Distribution Parameters

It is easily understood that the Gamma distribution does not work properly fitting the whole range of the spectrum of statistical and jet-induced contributions. As the shape of the right-hand side is to some extend similar to the shape of the purely statistical case, a second kind of parametrization may be given by the Gamma distribution describing the right-hand side.
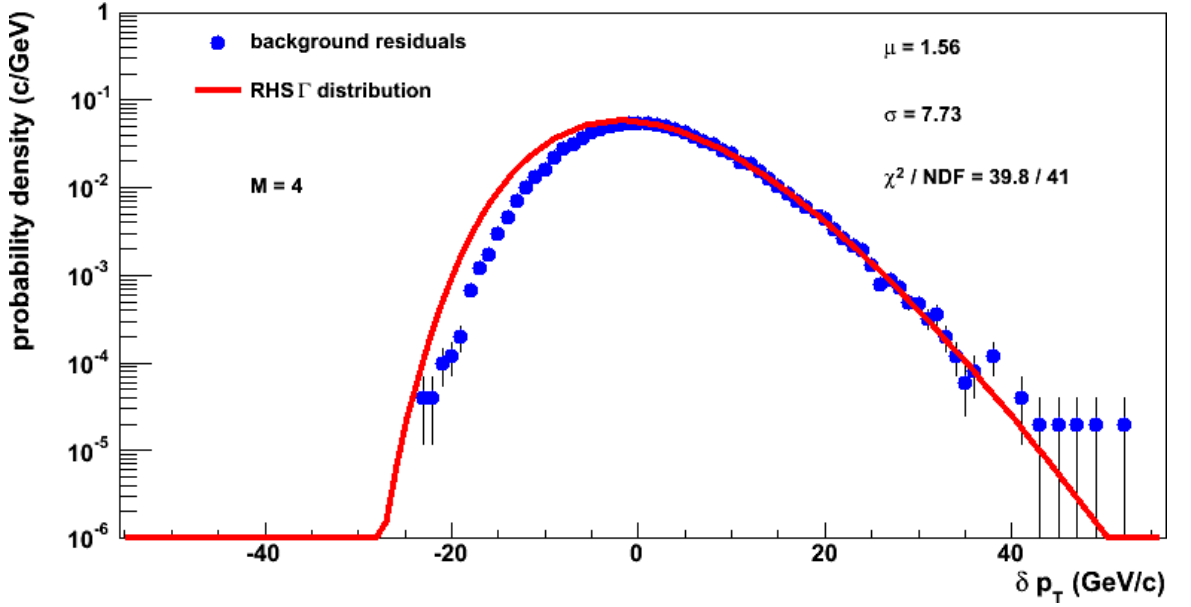
Figure 25: *The Gamma distribution fitted to the right-hand side of the experimentally found background residual spectrum for M = 4. Denoted are the mean μ and the standard deviation σ of the residual distribution and the χ^2/NDF of the fit.*

In fact, with a χ^2/NDF ranging from 0.63 to 1.37 for multiplicity classes of $M \geq 2$ the Gamma distribution works for a parametrization of the right-hand side. A counterpoint to this is the fact that all parameters p, b, A vary. For the case of the left-hand side fit the parameter a was stable, b was fixed by purpose leaving p the only variable necessary. Making a similar approach fixing the parameter b for instance results in bad χ^2/NDF for most of the multiplicity classes. These observations make clear that with the jet-induced contributions the fluctuations do not have the statistical character as the fluctuations on the left-hand side, where the parameters follow a simple pattern ($b = a = $ const, $p \propto m$).

6 Summary

The subject of this work has been the characterization of the jet-induced background of Pb-Pb collisions at $\sqrt{s_{\text{NN}}} = 2,75\,\text{TeV}$. The aim was to parametrize the background residual spectra that were gained from track embedding and subsequent anti-k_T clustering. For that purpose the assumption was made that the spectra consist of a purely statistical part and a contribution of jets that only affects the right-hand side of the spectra (energies contributed by jets are positive).

In order to describe the purely statistical fraction of these background residuals the Gamma distribution has been introduced. An artificial background residual spectrum of independent emission had been simulated which has successfully been described by the Gamma distribution. Therefore the Gamma distribution has found to be valid for the description of background fluctuations of mere statistical nature.

The fit parameters of the Gamma distribution followed the expected pattern and the fraction p/b provided an even stabler parameter. In addition, a correction factor κ has been found that translates p/b into the mean transverse momentum $< p_T >$. Since the Gamma distribution has successfully described the whole spectrum fitting only the left-hand side, it can be used to determine the statistical part of the real background residual spectrum. In doing so, it was noticed that the parameters differ slightly from the simulated case showing that an additional sort of fluctuation has to be considered for a definite analysis.

A characterization of the background influence in jet reconstruction is given by the exponential function (Eq.(34)) with the parameters that can be found in the appendix (cf. tabular 5). With this function the ratio of jet-induced to purely statistical fluctuation has successfully been parametrized. A brief insight into the parameters of the exponential fit showed that they both seem to follow a second order polynomial for varying multiplicities. Nevertheless the data points at this point are too few to gain a definite function describing the correction fit as a function of the multiplicity exclusively.

In the scope of general jet analysis the given parametrization can be used to quantify the relative influence of the jet-induced background, namely by deconvolution of jet spectra with the spectrum of background fluctuations. In matters of the QGP analysis, this can lead to more quantitative conclusions about the influence of medium-induced effects like the dijet-imbalance.

In this work it had been assumed that the fluctuations on the left-hand side of the residual spectrum are purely statistical and the only disturbance was expected from jet-induced contributions at the right-hand side. A continuation to this work may take additional effects into consideration like the elliptic flow.

References

[A+10] Georges Aad et al. Observation of a Centrality-Dependent Dijet Asymmetry in Lead-Lead Collisions at $\sqrt{s_{NN}}$= 2.76 TeV with the ATLAS Detector at the LHC. *Phys.Rev.Lett.*, 105:252303, 2010.

[C+08] Mateo Cacciari et al. The anti-kt jet clustering algorithm. 2008.

[GO09] Jan-Fiete Große-Oetringhaus. *Measurement of the Charged-Particle Multiplicity in Proton-Proton Collisions with the ALICE Detector*. Doktorarbeit, Institut für Kernphysik, University of Muenster, Germany, Muenster, 2009.

[KB11] Christian Klein-Bösing. Jet reconstruction and jet background classification with the alice experiment in pb-pb collisions at the lhc. *arXiv:1106.4303*, 2011.

[M+07] Miller et al. Glauber Modeling in High Energy Nuclear Collisions. *Annu. Rev. Nucl. Part. Sci.*, 57:205–243, 2007.

[MT01] M.J. and Tannenbaum. The distribution function of the event-by-event average pt for statistically independent emission. *Physics Letters B*, 498(1-2):29 – 34, 2001.

[Oet11] Jan Fiete Große Oetringhaus. Latest results from the lhc: Heavy-ion physics. CTAN: https://indico.cern.ch/getFile.py/access?contribId=1&resId=1&materialId=slides&confId=135933, august 2011.

[Sal10] Gavin P. Salam. Towards jetography. *European Physical Journal C*, 67:1–29, 2010.

[Sal11] Gavin P. Salam. *Jets at Hadron Colliders*, march 2011. CTAN: https://indico.cern.ch/conferenceDisplay.py?confId=115078.

7 Appendix

7.1 Parametrization Data of the Statistically Independent Residual Spectra

Table 1: *Parameters gained from the left-hand side ($p_T \in [-70,0]$) Gamma distribution (Eq.(28)) fit of the statistically independent residuals δp_T.*

mult. class	p	b $(\text{GeV}/c)^{-1}$	p/b (GeV/c)	$A \cdot 10^5$	χ^2/NDF
0	7.9 ± 0.1	$1,85 \pm 0.01$	4.3 ± 0.1	0.992 ± 0.003	4542 / 3
1	25.0 ± 0.1	1.85 ± 0.01	13.5 ± 0.1	$1,008 \pm 0.003$	39.6 / 7
2	37.0 ± 1.9	1.70 ± 0.05	21.8 ± 1.3	$1,002 \pm 0.003$	15.3 / 10
3	45.3 ± 2.6	1.55 ± 0.05	29.2 ± 2.0	1.001 ± 0.003	7.9 / 14
4	54.7 ± 3.4	1.51 ± 0.05	36.2 ± 2.6	1.000 ± 0.003	19.7 / 17
5	69.0 ± 5.1	1.52 ± 0.06	45.4 ± 3.6	1.000 ± 0.003	24.9 / 20
6	74.0 ± 5.7	1.44 ± 0.06	51.4 ± 4.6	0.999 ± 0.003	25.6 / 20
7	109.1 ± 10.5	1.64 ± 0.09	66.5 ± 7.4	1.004 ± 0.003	16.9 / 22
8	110.3 ± 10.7	1.54 ± 0.08	71.6 ± 7.9	1.001 ± 0.003	11.2 / 23
9	122.7 ± 12.9	1.53 ± 0.09	80.2 ± 9.7	0.995 ± 0.003	26.2 / 26
10	125.7 ± 13.3	1.47 ± 0.08	85.5 ± 10.2	0.997 ± 0.003	29.7 / 27
11	149.3 ± 16.9	1.54 ± 0.09	96.9 ± 12.4	1.000 ± 0.003	25.2 / 29
12	182.7 ± 23.7	1.64 ± 0.11	111.4 ± 16.3	0.997 ± 0.003	26.7 / 30
13	169.9 ± 20.1	1.52 ± 0.10	111.8 ± 15.2	0.997 ± 0.003	33.6 / 31
14	196.8 ± 27.0	1.58 ± 0.11	124.6 ± 19.2	$1,001 \pm 0.003$	29.2 / 34
15	198.0 ± 27.9	1.53 ± 0.11	129.4 ± 20.5	0.999 ± 0.003	28.3 / 35
16	167.2 ± 20.5	1.37 ± 0.09	122.0 ± 17.0	0.997 ± 0.003	29.9 / 37

Table 2: *Parameters gained from the full range ($p_T \in [-70, 70]$) Gamma distribution (Eq.(28)) fit of the statistically independent residuals δp_T.*

mult. class	p	b $(\text{GeV}/c)^{-1}$	p/b (GeV/c)	$A \cdot 10^5$	χ^2/NDF
0	8.1 ± 0.1	1.85 ± 0.01	4.4 ± 0.1	0.978 ± 0.002	5453 ± 17
1	19.8 ± 0.5	1.63 ± 0.03	12.9 ± 0.3	0.999 ± 0.002	176.8 ± 25
2	32.9 ± 1.0	1.54 ± 0.03	21.2 ± 0.8	1.000 ± 0.002	47.7 ± 32
3	45.8 ± 1.5	1.55 ± 0.03	30.6 ± 1.2	1.000 ± 0.002	33.4 ± 39
4	56.8 ± 2.1	1.55 ± 0.03	39.7 ± 1.6	1.000 ± 0.002	47.4 ± 44
5	67.5 ± 2.7	1.52 ± 0.04	48.8 ± 2.2	1.000 ± 0.002	55.6 ± 50
6	83.3 ± 3.7	1.53 ± 0.04	57.5 ± 2.8	1.000 ± 0.002	55.2 ± 54
7	99.4 ± 4.9	1.53 ± 0.04	66.9 ± 3.6	1.000 ± 0.002	61.6 ± 55
8	103.1 ± 5.2	1.56 ± 0.04	77.0 ± 4.0	1.000 ± 0.002	37.5 ± 56
9	129.1 ± 7.1	1.50 ± 0.05	83.5 ± 5.3	1.000 ± 0.002	57.7 ± 64
10	138.5 ± 8.1	1.59 ± 0.05	96.5 ± 6.0	1.000 ± 0.002	78.2 ± 66
11	157.3 ± 9.5	1.53 ± 0.05	102.1 ± 6.8	1.000 ± 0.002	64.3 ± 70
12	185.1 ± 12.6	1.65 ± 0.06	118.4 ± 8.7	1.000 ± 0.002	73.6 ± 72
13	179.8 ± 11.7	1.54 ± 0.06	120.1 ± 8.8	1.000 ± 0.002	91.2 ± 72
14	193.8 ± 13.0	1.60 ± 0.06	133.3 ± 9.6	1.000 ± 0.002	70.1 ± 77
15	222.8 ± 16.6	1.69 ± 0.07	148.1 ± 11.8	1.000 ± 0.002	77.8 ± 79
16	216.4 ± 12.1	1.69 ± 0.05	148.1 ± 8.9	1.000 ± 0.002	74.7 ± 82

7.2 Parametrization Data of the Experimentally Found Residual Spectra

Table 3: *Parameters gained from the right-hand side ($p_T \in [0,70]$) Gamma distribution (Eq.(28)) fit of the residuals δp_T found in experimental data.*

mult. class	p	b $(\mathrm{GeV}/c)^{-1}$	p/b (GeV/c)	A	χ^2/NDF
0	2.0 ± 0.1	0.80 ± 0.01	$2.5 \pm$	1.38 ± 0.01	503.3 ± 28
1	7.0 ± 0.5	0.68 ± 0.02	$10.3 \pm$	1.22 ± 0.01	87.3 ± 35
2	11.8 ± 1.0	0.61 ± 0.03	$19.3 \pm$	1.19 ± 0.01	39.6 ± 40
3	130.8 ± 2.4	0.63 ± 0.04	$32.1 \pm$	1.17 ± 0.01	25.1 ± 40
4	19.7 ± 2.6	0.54 ± 0.04	$36.6 \pm$	1.17 ± 0.01	39.8 ± 41
5	47.6 ± 9.3	0.74 ± 0.07	$64.3 \pm$	1.13 ± 0.01	43.4 ± 43
6	43.4 ± 8.8	0.65 ± 0.07	$66.8 \pm$	1.14 ± 0.01	51.6 ± 49
7	47.8 ± 10.5	0.66 ± 0.07	$72.4 \pm$	1.13 ± 0.01	69.6 ± 51
8	109.3 ± 36.1	0.95 ± 0.15	$115.1 \pm$	1.12 ± 0.01	46.8 ± 50
9	186.6 ± 84.3	1.21 ± 0.26	$154.2 \pm$	1.13 ± 0.01	39.9 ± 45
10	59.3 ± 17.2	0.69 ± 0.10	$85.9 \pm$	1.13 ± 0.02	52.8 ± 48
11	312.9 ± 239.5	1.55 ± 0.58	$201.9 \pm$	1.12 ± 0.02	50.8 ± 45
12	804.9 ± 2861.7	2.37 ± 4.30	$339.6 \pm$	1.12 ± 0.04	25.5 ± 38

Table 4: *Parameters gained from the left-hand side ($p_T \in [-70,0]$) Gamma distribution (Eq.(28)) fit of the residuals δp_T found in experimental data.*

mult. class	p	p/b (GeV/c)	A	χ^2/NDF
1	21.8 ± 0.2	$14.0 \pm$	0.85 ± 0.01	386.3 ± 10
2	44.6 ± 0.4	$28.8 \pm$	0.86 ± 0.01	63.7 ± 15
3	71.6 ± 0.6	$46.3 \pm$	0.87 ± 0.01	21.2 ± 19
4	100.7 ± 0.9	$65.0 \pm$	0.88 ± 0.01	19.3 ± 22
5	129.6 ± 1.2	$83.6 \pm$	0.88 ± 0.01	19.4 ± 24
6	156.8 ± 1.6	$101.2 \pm$	0.88 ± 0.01	22.7 ± 28
7	178.9 ± 2.1	$115.4 \pm$	0.88 ± 0.01	31.9 ± 30
8	195.7 ± 2.2	$126.3 \pm$	0.88 ± 0.01	43.6 ± 32
9	212.8 ± 2.7	$137.3 \pm$	0.88 ± 0.01	31.5 ± 32
10	216.9 ± 2.9	$139.9 \pm$	0.89 ± 0.01	41.8 ± 37
11	221.2 ± 3.4	$142.7 \pm$	0.88 ± 0.01	33.9 ± 34
12	232.3 ± 10.4	$150.0 \pm$	0.90 ± 0.01	31.6 ± 32
$b = const = 1.55\,(\mathrm{GeV}/c)^{-1}$				

Table 5: *Parameters of the correction exponential function (Eq.([34])).*

mult. class	$\lambda \cdot 10^{-3}$	μ	χ^2/NDF
1	397 ± 4	6.2 ± 0.1	59.7 / 36
2	319 ± 3	8.8 ± 0.1	83.2 / 41
3	258 ± 3	11.1 ± 0.1	60.9 / 41
4	226 ± 3	13.5 ± 0.1	61.7 / 42
5	195 ± 3	15.5 ± 0.2	89.3 / 44
6	174 ± 3	16.8 ± 0.2	64.4 / 50
7	157 ± 3	18.6 ± 0.2	76.9 / 52
8	143 ± 4	19.6 ± 0.2	62.3 / 51
9	123 ± 4	20.6 ± 0.3	49.5 / 46
10	134 ± 4	21.3 ± 0.3	54.5 / 49
11	115 ± 4	21.4 ± 0.4	55.0 / 46
12	124 ± 12	21.8 ± 0.9	27.2 / 39

Table 6: *Parameters of the correction power law function (Eq.([33])).*

mult. class	a	b	n	χ^2/NDF
2	1.06 ± 0.01	3.02 ± 0.52	3.77 ± 8	245.1 / 40
3	1.06 ± 0.01	1.90 ± 0.44	3.60 ± 9	157.8 / 40
4	1.07 ± 0.01	1.10 ± 0.33	3.52 ± 11	120.0 / 41
5	1.05 ± 0.01	2.04 ± 0.63	3.14 ± 11	86.0 / 43
6	1.06 ± 0.02	0.49 ± 0.18	3.56 ± 13	98.3 / 49
7	1.07 ± 0.02	0.32 ± 0.13	3.58 ± 14	80.1 / 51
8	1.05 ± 0.02	1.28 ± 0.56	3.07 ± 14	71.3 / 49
9	1.09 ± 0.02	1.78 ± 0.81	2.89 ± 15	44.3 / 45
10	1.08 ± 0.02	0.42 ± 0.23	3.33 ± 17	65.0 / 48
11	1.11 ± 0.02	0.32 ± 0.20	2.66 ± 20	56.9 / 45
12	1.11 ± 0.06	0.69 ± 1.13	2.44 ± 53	26.9 / 38

7.3 Corrigendum

There have been two errors in the original version of this bachelor thesis (21.09.2011). Both errors concern mistakes in equations. However, all computations were still carried out with the right equations, only the representations of the equations were flawed.

- On page 20 the Gamma distribution has been redesigned to fit the problem of δp_T being located around zero. In order to displace the momentum, the replacement $p_T \to p_T - p/b$ has been made, which is wrong with $\delta p_T = p_T$. The right substitution (with $p_T := \delta p_T$ now) is $p_T \to \delta p_T + p/b$. Accordingly the formula (Eq.(28)) changes from

$$a \cdot f(p,b,p_T - \frac{p}{b}) = g(p,b,p_T,a) = \frac{ab}{\Gamma(p)} \left[b(p_T - \frac{p}{b}) \right]^{p-1} e^{-b(p_T - \frac{p}{b})}$$

  to the following right version:

$$a \cdot f(p,b,\delta p_T + \frac{p}{b}) = g(p,b,\delta p_T,a) = \frac{ab}{\Gamma(p)} \left[b(\delta p_T + \frac{p}{b}) \right]^{p-1} e^{-b(\delta p_T + \frac{p}{b})}$$

- On page 26 a formula for the mean momentum has been given (Eq.(36)). In the original version the correction factor κ has been misplaced. The wrong version is

$$< p_T >_{p/b} = \frac{p}{b} \cdot \kappa \cdot \frac{1}{m} \cdot \frac{2\pi\eta_{ac}}{\pi R^2}$$

  and has been replaced with the right version:

$$< p_T >_{p/b} = \frac{p}{b} \cdot \frac{1}{\kappa} \cdot \frac{1}{m} \cdot \frac{2\pi\eta_{ac}}{\pi R^2}$$

This version (27.10.2011) of the thesis already contains the corrections. The two flawed pages of the original version are presented in the following. Note, that the page numbers and equation numbers differ from the original version to preserve an unambiguous labeling.

5.2 Parametrization of Background Residuals of Statistically Independent Emission

In order to parametrize the distributions of independent emission the Gamma distribution (Eq.(15)) will be used. Additionally, a simple proportionality factor a is appended and the mean $\mu = p/b$ (Eq.(18)) is subtracted for the distribution to be peaked around zero:

$$a \cdot f(p, b, p_T - \frac{p}{b}) = g(p, b, p_T, a) = \frac{ab}{\Gamma(p)} \left[b(p_T - \frac{p}{b}) \right]^{p-1} e^{-b(p_T - \frac{p}{b})} \qquad (36)$$
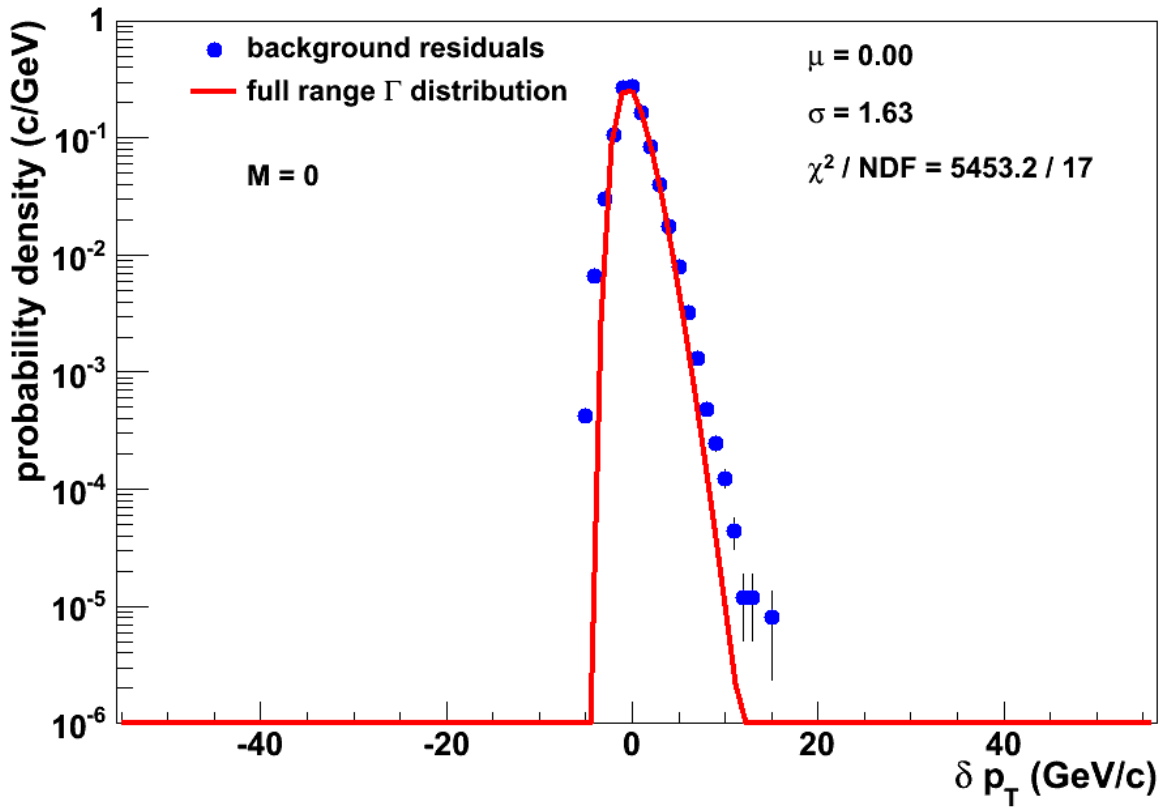

Figure 26: *Illustration of the Gamma distribution fitted to the residual spectrum for the multiplicity class $M = 0$. Denoted are the mean μ and the standard deviation σ of the residual distribution and the χ^2/NDF of the fit.*

Though the fit of the Gamma distribution was computed for the whole range, it does not work well for the smallest multiplicity class $M = 0$ with $\chi^2/NDF \approx 321$ due to a low number of supporting points (cf. figure 26). For $M = 1$ the fit has improved with $\chi^2/NDF \approx 7$ and for the rest of the classes χ^2/NDF only ranges from 0.67 to 1.49.
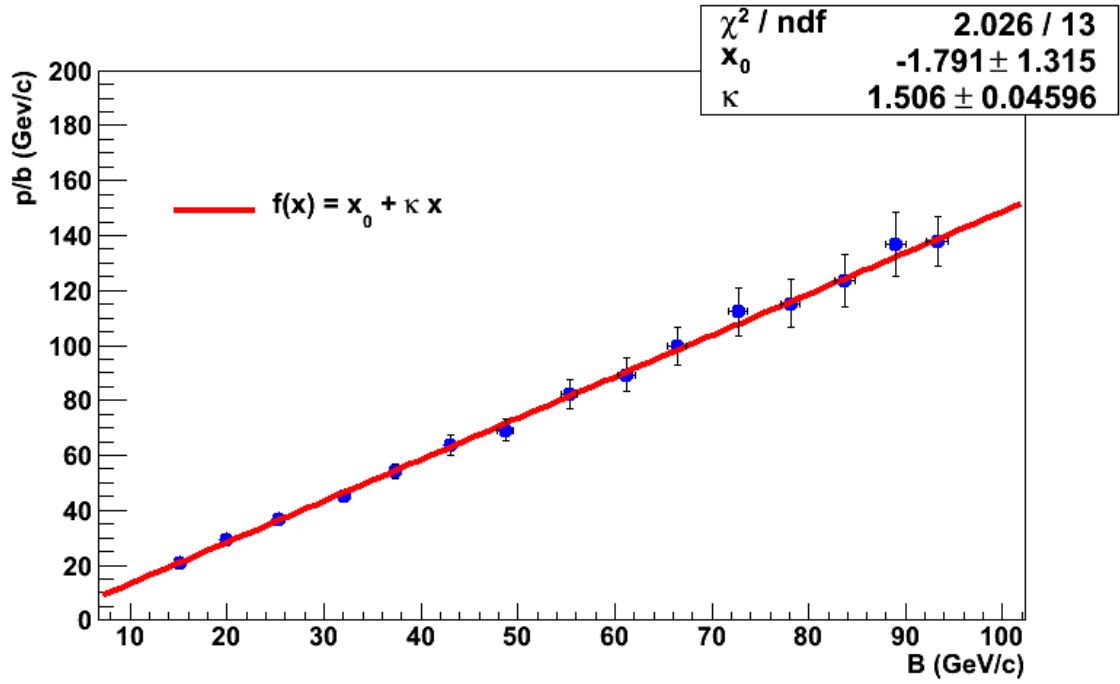
Figure 27: *Correlation of p/b and B. Denoted are the parameters and the χ^2/NDF of the fit function.*

In figure 27 p/b is plotted against B for the given multiplicity classes.[6] The ratio of both is not unity, as it would be expected for a non-truncated single particle track spectrum. Nevertheless, with the slope $\kappa = 1.51 \pm 0.05$ a correction factor is given. Divided by the multiplicity m and with undoing the adjustment for the track acceptance and clustering area, $p/b \cdot \kappa$ should provide the $< p_T >$ of the single track spectrum:

$$< p_T >_{p/b} = \frac{p}{b} \cdot \kappa \cdot \frac{1}{m} \cdot \frac{2\pi\eta_{\text{ac}}}{\pi R^2} \tag{37}$$

E.g. with $M = 9$ with $m \approx 1900$ the resulting $< p_T >_{p/b} = 0.65\,\text{GeV/c} \pm 0.05\,\text{GeV/c}$[7] matches the mean momentum of the single tracks $< p_T >= 0.65\,\text{GeV/c} \pm 0.44\,\text{GeV/c}$. Thereby, the parameter p/b with the factor κ remains a valid expression for the mean momentum.

---

[6]Like for p/b in figure 17, the χ^2/NDF seems again too low with approx. 0.15. It is to recall that the uncertainty was estimated too high due to the dependency of p and b.

[7]The uncertainty of $< p_T >_{p/b}$ was estimated with the uncertainty of p/b.

Danksagung

Ich möchte den Verantwortlichen der Arbeitsgruppe Wessels dafür danken, dass sie mir eine Bachelorarbeit auf dem Gebiet der Kernphysik ermöglicht haben. Besonders bedanke ich mich bei Dr. Christian Klein-Bösing und Bastian Bathen für die Betreuung.

Hiermit bestätige ich, dass ich diese Arbeit selbstständig verfasst und keine anderen als die angegebenen Quellen und Hilfsmittel verwendet habe.

Münster, 21.09.2011

Hendrik Poppenborg